Flow in the western Mediterranean shallow mantle: Insights from xenoliths in Pliocene alkali basalts from SE Iberia (eastern Betics, Spain)

Karoly Hidas, Zoltan Konc, Carlos J. Garrido, Andrea Tommasi, Alain Vauchez, Jose Alberto Padron Navarta, Claudio Marchesi, Guillermo Booth-Rea, Antonio Acosta-Vigil, Csaba Szabo, et al.

AGU PUBLICATIONS

Tectonics

RESEARCH ARTICLE
10.1002/2016TC004165

Károly Hidas and Zoltán Konc contributed equally to this work.

Key Points:
- SE Iberian mantle xenoliths record deformation that is consistent with transtensional regime
- Deformation and melt-mediated recovery of SE Iberian mantle xenoliths is Neogene in age
- Seismic anisotropy data in SE Iberia can be explained by steeply dipping foliation and subhorizontal lineation of the SCLM, with ENE strike

Supporting Information:
- Figures S1–S3

Correspondence to:
K. Hidas,
karoly.hidas@csic.es

Citation:
Hidas, K., et al. (2016), Flow in the western Mediterranean shallow mantle: Insights from xenoliths in Pliocene alkali basalts from SE Iberia (eastern Betics, Spain), *Tectonics*, *35*, 2657–2676, doi:10.1002/2016TC004165.

Received 26 FEB 2016
Accepted 26 OCT 2016
Accepted article online 2 NOV 2016
Published online 25 NOV 2016

Flow in the western Mediterranean shallow mantle: Insights from xenoliths in Pliocene alkali basalts from SE Iberia (eastern Betics, Spain)

Károly Hidas[1], Zoltán Konc[1], Carlos J. Garrido[1], Andréa Tommasi[2], Alain Vauchez[2], José Alberto Padrón-Navarta[2], Claudio Marchesi[1,3], Guillermo Booth-Rea[1,4], Antonio Acosta-Vigil[1], Csaba Szabó[5], María Isabel Varas-Reus[1], and Fernando Gervilla[1,3]

[1]Instituto Andaluz de Ciencias de la Tierra, CSIC and UGR, Granada, Spain, [2]Géosciences Montpellier, Université de Montpellier and CNRS, Montpellier, France, [3]Departamento de Mineralogía y Petrología, Universidad de Granada, Granada, Spain, [4]Departamento de Geodínamica, Universidad de Granada, Granada, Spain, [5]Lithosphere Fluid Research Laboratory, IGES, Eötvös Loránd University, Budapest, Hungary

Abstract Mantle xenoliths in Pliocene alkali basalts of the eastern Betics (SE Iberia, Spain) are spinel ± plagioclase lherzolite, with minor harzburgite and wehrlite, displaying porphyroclastic or equigranular textures. Equigranular peridotites have olivine crystal preferred orientation (CPO) patterns similar to those of porphyroclastic xenoliths but slightly more dispersed. Olivine CPO shows [100]-fiber patterns characterized by strong alignment of [100]-axes subparallel to the stretching lineation and a girdle distribution of [010]-axes normal to it. This pattern is consistent with simple shear or transtensional deformation accommodated by dislocation creep. One xenolith provides evidence for synkinematic reactive percolation of subduction-related Si-rich melts/fluids that resulted in oriented crystallization of orthopyroxene. Despite a seemingly undeformed microstructure, the CPO in orthopyroxenite veins in composite xenoliths is identical to those of pyroxenes in the host peridotite, suggesting late-kinematic crystallization. Based on these observations, we propose that the annealing producing the equigranular microstructures was triggered by melt percolation in the shallow subcontinental lithospheric mantle coeval to the late Neogene formation of veins in composite xenoliths. Calculated seismic properties are characterized by fast propagation of *P* waves and polarization of fast *S* waves parallel to olivine [100]-axis (stretching lineation). These data are compatible with present-day seismic anisotropy observations in SE Iberia if the foliations in the lithospheric mantle are steeply dipping and lineations are subhorizontal with ENE strike, implying dominantly horizontal mantle flow in the ENE-WSW direction within vertical planes, that is, subparallel to the paleo-Iberian margin. The measured anisotropy could thus reflect a lithospheric fabric due to strike-slip deformation in the late Miocene in the context of WSW tearing of the subducted south Iberian margin lithosphere.

1. Introduction

The Betics and the Rif form a tight arc-shaped mountain belt of the Alpine orogenic system in the westernmost Mediterranean, surrounding the Alborán Sea basin. This orogenic belt is a result of the Miocene collision between the Alborán domain and the south Iberian and Maghrebian passive margins in the context of N-S to NW-SE convergence of the African and the European plates. Slab rollback and break off, mantle lithosphere delamination, and convective thinning of overthickened lithospheric roots are among the diverse geodynamic scenarios proposed to account for Tertiary synorogenic extension that led to the opening of the Alborán Sea basin and resulted in the current shape and topography of the orogenic belt [e.g., *Platt et al*., 2013, and references therein]. An increasing number of recent seismological surveys have investigated the current deep mantle structure of the Betics-Rif arc aiming to elucidate its Tertiary geodynamic evolution [e.g., *Buontempo et al*., 2008; *Calvert et al*., 2000; *Diaz et al*., 2010; *Serrano et al*., 2005]. Among these, teleseismic shear wave splitting measurements show that the fast direction of shear wave splitting (SKS) splitting is parallel to the limbs of the Betics-Rif arc and rotates around the Gibraltar arc [*Buontempo et al*., 2008; *Diaz et al*., 2010]. Although these data have been used to support geodynamic hypotheses proposing rollback of a westward retreating slab, the nature, age, and geodynamic significance of this seismic anisotropy are still uncertain. Combination of fossil anisotropy from Eocene subduction and renewed Miocene asthenospheric

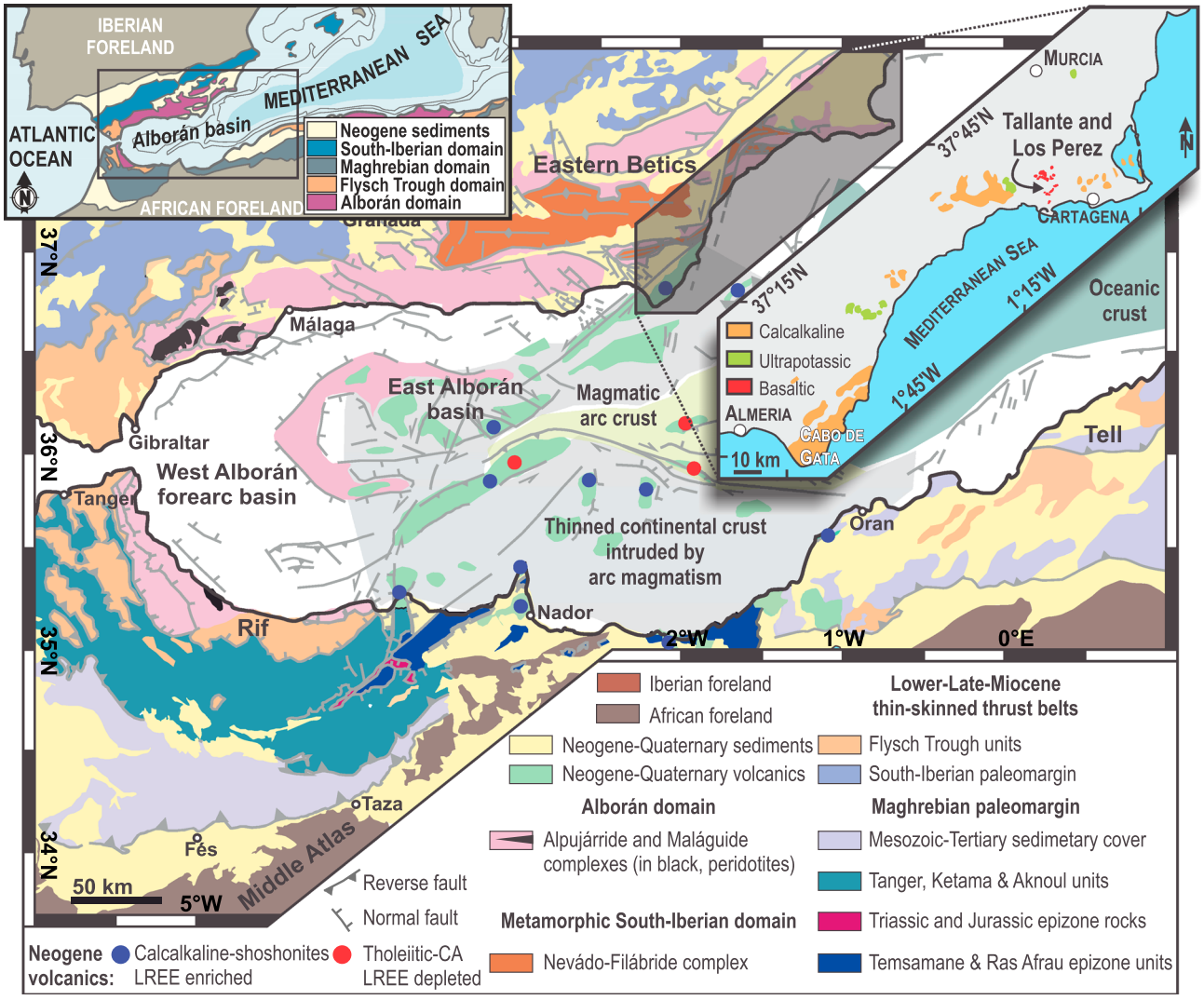

Figure 1. Simplified geological map of the westernmost Mediterranean termination of the circum-Mediterranean Alpine belt, showing the main tectonic domains of the Betics-Rif orogenic belt with the areas of oceanic crust, magmatic arc, and thin continental crust in the Alborán basin (modified after *Booth-Rea et al.* [2007, and references therein]). The inset corresponds to the South East Iberian Volcanic Province in the eastern Betics, showing the distribution of different types of Miocene to Pliocene volcanism and the location of the Tallante and Los Perez alkali basalt volcanic centers that host the studied mantle xenoliths (modified after *Cebriá et al.* [2009]).

flow around an Alborán slab is among the hypotheses put forward to account for the seismic anisotropy in the circum-Alborán Sea basin. Some difficulties in the interpretation of SKS measurements arise from deciphering if the source of anisotropy is in the lithosphere or asthenosphere [e.g., *Silver*, 1996]. Laboratory and theoretical studies indicate that seismic anisotropy in the uppermost mantle results mainly from the crystal preferred orientation (CPO) of mantle olivine [*Nicolas and Christensen*, 1987; *Silver et al.*, 1999; *Tommasi et al.*, 2000; *Zhang and Karato*, 1995]. Microstructural studies of natural mantle peridotites hence can provide useful information on the nature and significance of the upper mantle seismic anisotropy [e.g., *Mainprice and Silver*, 1993; *Mainprice et al.*, 2000].

Pliocene alkali basalts in the inner easternmost Betics (Figure 1a) entrained numerous mantle xenoliths that provide a unique opportunity for direct observation of the microstructures and composition of the lithospheric mantle 2–3 Ma ago [e.g., *Bianchini et al.*, 2011; *Capedri et al.*, 1989; *Rampone et al.*, 2010]. Here we report a detailed microstructural and CPO study of mantle spinel peridotite xenoliths from the Tallante area volcanic centers (Murcia, SE Spain) in order to unravel the deformation record, constrain the relative age of

microstructures, and derive the anisotropic seismic properties of the lithospheric mantle beneath SE Iberia. Comparison of the calculated anisotropy to available seismic data provides insights into the source and significance of seismic anisotropy in the NE termination of the Alborán arc system.

2. Tectonic Setting and Cenozoic Volcanism

The Betics-Rif orogen in the westernmost Mediterranean (Figure 1a) was formed during the Miocene collision between the Alborán domain and the south Iberian and Maghrebian passive margins in the context of Africa-Iberia convergence [*Booth-Rea et al*., 2007; *Jolivet and Faccenna*, 2000]. Among other features, this arched orogenic belt is characterized by series of nappes of metamorphic rocks, which contain slivers of subcontinental lithospheric peridotites [*Garrido et al*., 2011; *Obata*, 1980; *Van der Wal and Vissers*, 1996], and Cenozoic arc-like volcanism [*Duggen et al*., 2003, 2004, 2005; *Hoernle et al*., 1999; *Marchesi et al*., 2012; *Turner et al*., 1999] (Figure 1a).

Neogene to Quaternary volcanism occurred mainly in SE Iberia, the Maghrebian margins, and the present-day Alborán Sea basin (Figure 1a). In the early to middle Miocene this volcanic activity was broadly coeval with extension and subsidence of the Alborán Sea basin and orogenesis in the surrounding Betics-Rif mountain belt [*Booth-Rea et al*., 2007; *Comas et al*., 1999; *Jolivet and Faccenna*, 2000; *Lonergan and White*, 1997]. Middle to late Miocene tholeiitic through calc-alkaline volcanic rocks typical of subduction arc magmatism crop out across the central and eastern Alborán Sea basin (Figure 1a), in the Alborán Island, and in the coastal volcanic complexes at the margins of the eastern Betics—often referred to as the Southeast Iberian Volcanic Province (SEIVP) (Figure 1b)—and the Maghrebides (Figure 1a) [*Duggen et al*., 2004, 2005; *Turner et al*., 1999, and references therein]. In addition to this Neogene igneous activity, the SEIVP comprises late Miocene to Plio-Pleistocene shoshonitic igneous rocks and basanites/alkali basalts and their derivatives, often referred in the literature as anorogenic magmatism (Figure 1b) [e.g., *Duggen et al*., 2003, 2004, 2005; *Hoernle et al*., 1999; *Turner et al*., 1999]. Some alkali basalt volcanic centers contain numerous crustal/mantle high-grade metamorphic, mafic and ultramafic xenoliths, and megacrysts [e.g., *Bianchini et al*., 2015, and references therein].

Among other concurrent hypotheses [e.g., *Doblas et al*., 2007; *Turner et al*., 1999], late Miocene to Pliocene lithospheric decompression and coeval Si-K-rich magmatism and Quaternary alkali basalts in the SEIVP and Maghrebian margins have been related to subcontinental-edge delamination followed by asthenospheric mantle upwelling [*Duggen et al*., 2003, 2005, 2008] and/or earlier slab break off in the Algerian-Rifean margin [*Spakman and Wortel*, 2004, and references therein].

3. Provenance of the SE Iberian Subcontinental Lithospheric Mantle

The high $^{176}Hf/^{177}Hf$ and Lu/Hf ratios in clinopyroxene and peridotite whole rocks [*Bianchini et al*., 2011], the presence of clusters produced from garnet breakdown (Figures 2c and 2d) [*Rampone et al*., 2010; *Shimizu et al*., 2008], and the occurrence of plagioclase in SE Iberian mantle xenoliths (Table 1) [*Rampone et al*., 2010] indicate that the SE Iberian subcontinental lithospheric mantle (SCLM) was first equilibrated at minimum depths of 55–60 km, in the garnet lherzolite stability field, and it was later exhumed (in the sense of *England and Molnar* [1990]) and equilibrated in the plagioclase lherzolite facies. This corresponds to at least 30–40 km thinning of the SCLM (Figure 3). *Rampone et al*. [2010] argued for a prekinematic garnet breakdown based on the systematic orientation of orthopyroxene [100] cleavage planes in stretched clusters. This model involves thinning and decompression of the lithospheric mantle from garnet- to spinel-lherzolite facies conditions followed by ductile flow in the spinel to plagioclase facies.

The presence of metasomatic plagioclase indicates equilibration in the shallow mantle was accompanied by reactive melt percolation [*Bianchini et al*., 2011; *Kogarko et al*., 2001; *Rampone et al*., 2010; *Shimizu et al*., 2004]. The 0.7–0.9 GPa pressure estimation for both the formation of intrusive veins [*Bianchini et al*., 2015; *Rampone et al*., 2010] and that of Al, Cr, and Ti zoning in pyroxenes [*Kogarko et al*., 2001] point to an anomalously thin crust of 19–22 km above a hot SCLM at the time of eruption (2–3 Ma ago [*Duggen et al*., 2005]), which is consistent with the present-day crust-mantle boundary at $<$25 km beneath the region [*Mancilla et al*., 2015].

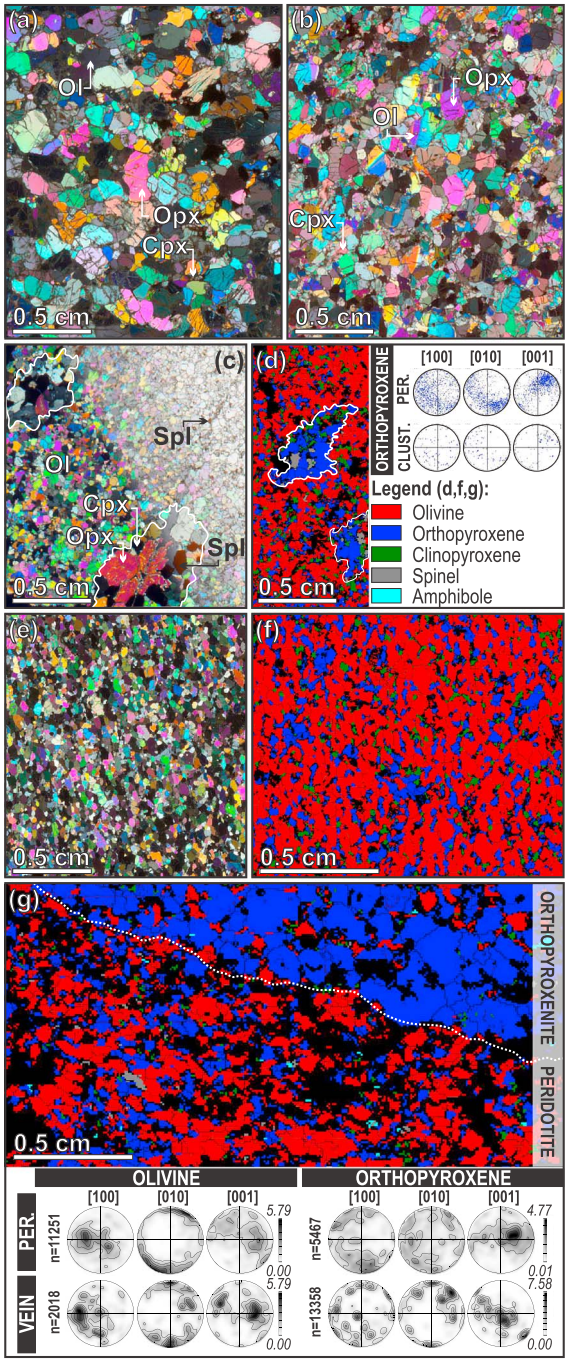

Figure 2. Photomicrographs and EBSD phase maps of the (a) granular (sample LPE-042), (b) porphyroclastic (sample TAL-047), (c and d) mosaic equigranular (sample LPE-002), and (e and f) flattened equigranular (sample LPE-025) textures of the SE Iberian mantle xenoliths. The microstructure of a representative composite xenolith (LPE-008) is shown in Figure 2g with the orthopyroxenite vein (top right) and the mosaic equigranular host peridotite (bottom left). The crystal preferred orientation (CPO) of olivine and orthopyroxene in the pyroxenite vein and in the peridotite is shown in the sample reference frame (i.e., without rotating the data to a common frame of reference such as those shown in Figure 4) in lower hemisphere equal area stereographic projections (contours at 0.5 multiples of a uniform distribution). Note the similarity of CPO between olivine-olivine and orthopyroxene-orthopyroxene pairs. In Figures 2c and 2d, ellipsoid-shaped, coarse-grained orthopyroxene-spinel clusters are outlined by white solid lines, and the identical distribution of orthopyroxene CPO in the clusters and the host peridotite (Figure 2d) is presented in lower hemisphere equal area stereographic projections in the sample reference frame (see above). The photomicrographs of Figures 2a, 2b, and 2e and the bottom left part of Figure 2c were taken using cross polarized light, whereas the top right part of Figure 2c using plane polarized light. Images in Figures 2d, 2f, and 2g are EBSD phase maps that share the same color coding shown in Figure 2d. Cpx: clinopyroxene; Ol: olivine; Opx: orthopyroxene; and Spl: spinel.

Table 1. Summary of Petrography, Modal Composition, Estimated Temperatures, Calculated Parameters, and the Significant Values of Seismic Properties

Sample	Lithology (Fabric)[a]	Modal Composition (%)					Estimated Temperature (°C)[b]			Calculated Parameters[b]					*Vp* (km/s)[c]		AVs (%)[c]	
		Ol	Opx	Cpx	Spl	Plag	T_{solv}	$T_{Ca\text{-}Opx}$	$T_{Al\text{-}Opx}$	BA	GOS	J_{Ol}	J_{Opx}	J_{Cpx}	min	max	min	max
Normal Mantle Xenoliths																		
LP08-12	WHR (ME)	81.0	0.3	17.9	0.9	-	-	-	-	0.57	0.9	2.2	-	3.0	8.03	8.61	0.21	4.32
LPE-002[d]	LHZ (ME)	66.9	21.0	10.3	1.7	<0.1	867	994	949	0.80	1.6	2.8	3.0	2.5	8.01	8.67	0.08	5.43
LPE-016[d]	LHZ (ME)	70.3	16.7	11.6	1.4	-	-	-	-	0.50	1.0	2.1	2.7	2.4	7.95	8.61	0.08	4.95
LPE-025	LHZ (TE)	77.3	17.0	5.7	0.0	-	-	-	-	0.76	1.3	5.2	1.4	2.3	7.97	8.90	0.16	6.85
LPE-028	WHR (ME)	85.9	0.4	13.7	0.0	-	-	-	-	0.59	1.1	2.6	-	2.9	7.98	8.69	0.10	5.82
LPE-029[d]	LHZ (ME)	69.7	19.3	7.9	2.9	0.2	986	1055	935	0.72	1.7	2.5	3.3	2.8	8.00	8.67	0.10	5.56
LPE-042[d,e]	LHZ (GR)	61.9	20.4	14.5	3.2	-	939	988	993	0.77	1.4	3.9	3.8	-	8.03	8.69	0.06	4.90
LPE-048[e]	LHZ (PO)	77.2	14.0	8.4	0.4	-	977	1047	969	0.74	2.2	4.3	-	4.6	7.98	8.80	0.12	7.22
LPE-058	LHZ (GR)	62.2	18.3	18.0	0.7	0.8	-	-	-	0.51	1.7	6.5	5.1	4.8	7.94	8.67	0.25	5.81
LPE-061	LHZ (ME)	79.0	8.2	7.6	1.8	3.5	859	1124	1083	0.75	1.2	3.3	4.4	3.3	7.99	8.70	0.10	5.81
LPE-062[e]	LHZ (PO)	63.5	22.0	12.7	1.8	-	1005	1054	976	0.83	1.7	3.8	3.0	2.8	8.05	8.66	0.21	4.32
TAL-001[d]	LHZ (TR)	75.4	15.2	8.3	1.1	-	872	980	933	0.47	1.8	4.6	3.8	4.4	7.93	8.71	0.29	6.31
TAL-047[e]	HZB (PO)	84.4	11.0	3.6	1.0	-	-	-	-	0.73	2.6	4.6	3.9	4.8	7.98	8.81	0.31	6.49
TAL-056[e]	LHZ (PO)	77.5	15.6	5.9	0.9	-	887	976	982	0.78	1.9	5.7	4.1	4.5	7.99	8.84	0.33	6.83
TAL-084	LHZ (TR)	76.2	16.4	5.0	2.4	-	892	955	1010	0.91	1.8	6.3	3.6	3.6	8.01	8.94	0.16	7.04
TAL-094	LHZ (GR)	76.9	17.6	5.0	0.4	<0.1	905	970	1063	0.72	2.0	8.3	5.3	4.8	7.96	8.89	0.12	6.83
TAL-106	LHZ (TR)	73.6	15.1	10.8	0.6	<0.1	-	-	-	0.56	2.7	7.2	4.4	-	7.91	8.81	0.41	7.10
TAL-112[d]	LHZ (ME)	74.7	13.8	8.6	2.9	-	884	956	945	0.63	1.3	2.0	3.0	2.9	8.02	8.60	0.08	4.61
TAL-124	HZB (PO)	87.0	10.3	2.3	0.4	<0.1	-	-	-	0.84	2.9	6.8	4.2	-	7.98	9.01	0.35	7.52
TAL-127	LHZ (PO)	70.7	20.0	8.0	1.3	<0.1	1038	951	994	0.66	1.9	5.1	2.6	2.7	7.96	8.75	0.21	6.30
TAL-134[d]	LHZ (ME)	67.2	18.3	12.9	1.6	-	843	974	962	0.63	1.1	2.4	4.5	-	8.00	8.61	0.17	4.70
TAL-148[f]	LHZ (PO)	68.7	13.7	9.6	1.5	2.9	-	-	-	0.58	2.7	4.7	4.0	4.2	7.97	8.73	0.31	6.09
Composite Mantle Xenoliths																		
LPE-008	WR (-)	40.3	57.1	2.0	0.6	<0.1	-	-	-	-	-				8.05	8.40	0.06	3.41
	HZB (ME)	65.3	31.5	2.2	1.0	-	-	-	-	0.56	1.3	3.3	2.2	-	-	-	-	-
	V (IG)	12.6	85.4	1.9	0.1	<0.1	-	-	-	-	-	-	-		-	-	-	-
TAL-014	WR (-)	63.3	28.6	4.5	0.1	3.5	-	-	-	-	-	-	-		8.08	8.56	0.14	3.91
	HZB (ME)	80.1	13.3	3.7	0.1	2.9	894	1175	1070	0.73	1.0	2.3	2.5	3.9	-	-	-	-
	V (IG)	11.8	75.6	7.1	-	5.5	-	-	-	-	-	-	-		-	-	-	-

[a]Lithology: HZB, harzburgite; LHZ, lherzolite; V, vein; WHR, wehrlite; WR, whole rock/(Fabric); GR: granular; IG, igneous; ME, mosaic equigranular; PO, porphyroclastic; TR, transitional; TE, tabular equigranular

[b]BA, BA index of olivine; GOS, area-weighted average of grain orientation spread of olivine (°); J_{Ol}, J_{Opx} and J_{Cpx} denote the CPO strength of olivine, orthopyroxene and clinopyroxene, respectively. T_{solv}: two-pyroxene temperature (±31°C), *Taylor* [1998]; $T_{Ca\text{-}Opx}$: Ca-in-orthopyroxene (±16°C), *Brey and Köhler* [1990]; and $T_{Al\text{-}Opx}$: Cr-Al-orthopyroxene (±15°C), *Witt-Eickschen and Seck* [1991].

[c]V_P is the calculated P wave velocity (km/s), and AVs is the anisotropy of S waves (%) owing to S wave splitting.

[d]Contains spinel-pyroxene cluster.

[e]Oriented thin section.

[f]Contains amphibole (3.7%).

4. Sampling Strategy

The mantle xenoliths collected for the present study come from the alkali basalt volcanic centers of "Cabezo Negro de Tallante," hereafter referred to as Tallante (12 samples with prefix TAL), and "Los Perez" (12 samples with prefixes LP08 or LPE) (Table 1), located northwest of Cartagena (Murcia, Spain) at 37°39′27″N/1°09′01″W and 37°39′59″N/1°08′12″W, respectively (Figure 1). We selected the samples on the basis of the lack of macroscopic evidence for contamination by host magma, their size, and their representativeness in terms of their macroscopic texture and modal composition. In the sample set we also include two composite xenoliths (LPE-008 and TAL-014) that contain several millimeter- to centimeter-wide veins of orthopyroxenite. Similar veins in the area have been interpreted as produced by silica-rich, subduction-derived mantle metasomatism [e.g., *Rampone et al*., 2010; *Shimizu et al*., 2008, and references therein], which predates the formation of kaersutitic amphibole veins, vein networks, and/or large amphibole-bearing patches that are also common in the Tallante volcanic center and have been interpreted as the precursors of alkaline basaltic volcanism [*Bianchini et al*., 2011, 2015; *Rampone et al*., 2010]. Therefore, the selected composite xenoliths might provide relative time constraints between the deformation recorded in peridotite and subduction-related metasomatism in the area.

Most xenoliths display no visible foliation and/or lineation, and thin sections were cut at random orientations. In the few samples where clear foliation is present and stretching lineation is defined by elongated spinels,

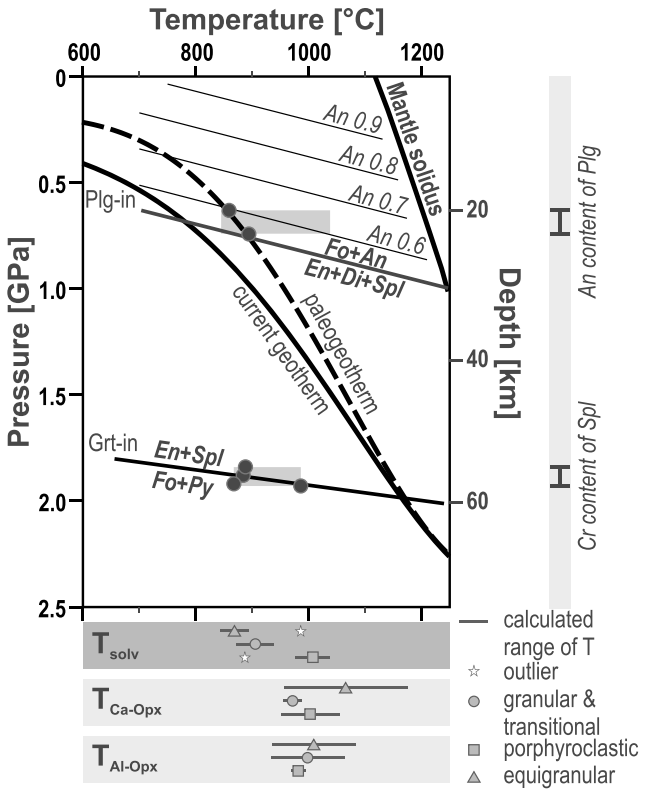

Figure 3. Pressure-temperature plot showing the range of temperatures and depths of equilibration of SE Iberian mantle xenoliths. Using geophysical temperature estimates of 700°C at the Moho and 1100°C at 45 km in the lithospheric mantle at the nearby Cartagena area [e.g., *Torné et al*., 2000], we estimate a geotherm that results in a high surface heat flow of 105 mW m^{-1}. This result is in line with published heat flow data in the eastern Betics, ranging up to 120 mW m^{-1} [e.g., *Torné et al*., 2000; *Negredo et al*., 2002, and references therein]. The solid black curve denotes the calculated geotherm, and the dashed black line is the paleogeotherm at the time of entrainment of mantle xenoliths by Pliocene alkali basalts [*Konc*, 2013]. The spinel-garnet peridotite transition (Grt-in solid line) in the Cr-CMAS system is calculated from the spinel composition [*O'Neill*, 1981] of cluster-bearing porphyroclastic peridotite xenoliths. The spinel-plagioclase lherzolite transition is shown for the CMAS system (Plg-in solid line) and in the Ti,Cr-NCFMAS system for different An-contents of plagioclase (An, labeled thin lines) [*Borghini et al*., 2010, 2011]. Brackets in the right side of the plots are the estimated initial minimum depth of equilibration in the spinel-garnet facies transition and the final equilibration depth of xenoliths in the plagioclase-spinel facies as deduced from spinel and plagioclase composition, respectively. See the geothermobarometry chapter for further details. Estimated ranges and average equilibrium temperature (T_{solv}, $T_{Ca\text{-}Opx}$, and $T_{Al\text{-}Opx}$) of different textural groups of xenoliths calculated using different geothermometric formulations are shown at the bottom of the figure (see text for details).

thin sections were cut perpendicular to foliation and parallel to lineation (XZ section). To improve the quality of electron backscatter diffraction (EBSD) measurements, standard diamond-polished (down to 0.25 μm grain size) thin sections were further polished for 5 min with a chemical-mechanical procedure using colloidal silica suspension (Buehler Mastermet).

5. Lithologies

The studied xenoliths are mainly spinel ± plagioclase lherzolites and, to a lesser extent, spinel-plagioclase harzburgites and spinel wehrlites (Table 1). Tallante xenoliths are lherzolites and harzburgites with lower clinopyroxene modal content than those of the Los Perez volcanic center. In the latter locality, in addition to rare wehrlites, sampled xenoliths are mostly lherzolites with variable clinopyroxene contents, including clinopyroxene-rich lherzolites with modal compositions near to that of the primitive mantle. The veins in the composite xenoliths (LPE-008 and TAL-014) are composed of pyroxenes, olivine, and spinel ± amphibole (Table 1), and they crosscut the spinel-plagioclase host peridotite. Interstitial accessory volatile-bearing minerals (mostly amphibole and apatite) are present in some samples (Table 1) and are similar to those reported in previous studies [e.g., *Bianchini et al*., 2011, 2015; *Rampone et al*., 2010; *Shimizu et al*., 2008].

6. Textures and Microstructures

The studied xenoliths are fine grained (≤1 mm) to coarse grained (≥3 mm) and have granular (3 samples, 13%), porphyroclastic (7 samples, 29%), or equigranular (11 samples, 45%) textures [cf. *Mercier and Nicolas*, 1975]. A few xenoliths show porphyroclast-to-granular transitional microstructures (three samples, 13%).

Granular peridotites are composed of uniformly coarse grains (up to centimeter) that have irregular shapes and lobate to straight grain boundaries. Olivine and pyroxenes typically show moderate intracrystalline deformation features, such as undulose extinction, subgrains, and/or kink bands (Figure 2a). Exsolution lamellae composed of clinopyroxene in orthopyroxene and orthopyroxene in clinopyroxene are common. Spinel is small, has irregular shapes, and is scattered in the samples.

Porphyroclastic peridotites are characterized by a weak bimodal grain size distribution with large, rounded orthopyroxene and, to a lesser extent, elongated olivine porphyroclasts embedded in a medium- to fine-grained recrystallized matrix of equiaxed or weakly elongated olivine, pyroxenes, and spinel (Figure 2b). Orthopyroxene porphyroclasts have irregular shapes with sutured grain boundaries and generally do not display intracrystalline deformation features. Olivine porphyroclasts have curvilinear to straight grain boundaries and, apart from occasional subgrain boundaries oriented normal to the crystal elongation direction, they do not show any intracrystalline plastic deformation features (Figure 2b). Similar to the granular xenoliths, exsolution lamellae of orthopyroxene in clinopyroxene and clinopyroxene in orthopyroxene are widespread. Spinel is generally rounded and interstitial. Where present, plagioclase occurs as polygonal aggregates rimming spinel or in elongated or rounded patches distributed subparallel to the foliation, with sharp boundaries to the surrounding matrix [cf. *Rampone et al*., 2010, and references therein].

Equigranular peridotite xenoliths display medium (1–3 mm) to fine-grained polygonal crystals of olivine and pyroxenes with straight boundaries and common 120° triple junctions (Figures 2c and 2d). Grains are free of intracrystalline deformation features or exsolution lamellae. Dark brown spinel crystals have irregular, cusped shapes and, less commonly, holly-leaf shapes filling interstices between silicates. The majority of the samples show mosaic equigranular texture with near equiaxed, polygonal grains. The lherzolite LPE-025 shows a tabular texture with elongated grains with aspect ratios up to 3:1 (Figures 2e and 2f).

In the composite xenoliths LPE-008 (Figure 2g) and TAL-014, the contact between veins and peridotite is serrated yet sharp. Unlike the fine-grained, strain-free mosaic equigranular wall peridotite, the orthopyroxenite veins mostly consist of coarse-grained, rounded orthopyroxenes (75–85 vol %, Table 1) that show an igneous texture with gently curved grain boundaries; they may contain exsolution lamellae of clinopyroxene and may also have undulose extinction. Smaller-sized olivine (11–12 vol %) and clinopyroxene (2–7 vol %), rare spinel (<0.1 vol %), and amphibole (<0.3 vol %) also occur in triple junctions in the veins (Figure 2g and Table 1). In Tallante, the orthopyroxenite veins contain minor interstitial plagioclase (5 vol %), which is also present in the host peridotite (Table 1).

Regardless of lithology or texture, some xenoliths contain clusters of coarse orthopyroxene (40–60 vol %) + clinopyroxene (20–35 vol %) + spinel (10–25 vol %) + olivine (<10 vol %). Clusters are best preserved in the equigranular xenoliths, where they have spherical or ellipsoidal shapes (Figures 2c and 2d). Occasionally, particularly in the porphyroclastic xenoliths, the clusters are stretched subparallel to the elongation direction of spinel in the host peridotite (i.e., in the foliation plane along the stretching lineation). Minerals in clusters are coarse grained, have straight grain boundaries, and show evidence of weak intragranular deformation and exsolution lamellae in pyroxenes. Similar clusters with akin modal compositions were described in previous studies [e.g., *Rampone et al*., 2010; *Shimizu et al*., 2008] and interpreted as the subsolidus breakdown of former garnet porphyroclasts based on the reaction of garnet + olivine ➔ spinel + orthopyroxene + clinopyroxene. We favor the same interpretation for the spinel + pyroxene clusters in the studied xenoliths.

7. Geothermobarometry

Details of electron microprobe analyses and the complete geochemical database are available in *Konc* [2013], here we only summarize the results of geothermobarometry (Table 1). The major element composition of minerals is nevertheless within the range previously reported in Tallante xenoliths [e.g., *Rampone et al*., 2010, and references therein].

The calculated equilibrium temperatures of peridotite xenoliths are obtained applying the two-pyroxene solvus (T_{solv}) [*Taylor*, 1998], the Ca-in-orthopyroxene ($T_{Ca\text{-}opx}$) [*Brey and Köhler*, 1990], and the Cr-Al-orthopyroxene ($T_{Al\text{-}opx}$) [*Witt-Eickschen and Seck*, 1991] geothermometers. The estimated uncertainty of these geothermometers given by the authors is ±16°C for the $T_{Ca\text{-}opx}$ and $T_{Al\text{-}opx}$, and ±31°C for the T_{solv}. Estimating temperatures for wehrlites was not possible due to the lack of accurate geothermometric formulation in clinopyroxene-olivine assemblages [cf. *Nimis and Grütter*, 2010]. We obtain a broad range of temperatures that show a weak correlation with the microstructures using the T_{solv} geothermometer (Table 1). The lowest temperatures in the range of 843–894°C are recorded in the equigranular textures, whereas the highest values, ranging from 1007 to 1038°C, were retrieved in the porphyroclastic ones, apart from one outlier in

each group (equigranular LPE-029: 986°C and porphyroclastic TAL-056: 887°C; Figure 3). The granular xenoliths record intermediate temperatures in the range of 905–939°C. The single pyroxene formulations provide higher values with an overlap for the different textural groups and lithologies in the range of 930–1177°C ($T_{Ca\text{-}in\text{-}Opx}$) and 933–1083°C ($T_{Cr\text{-}Al\text{-}Opx}$) (Table 1 and Figure 3). Apart from rare outliers, the cluster-bearing xenoliths record the lowest temperatures in the data set with T_{solv}, $T_{Ca\text{-}in\text{-}Opx}$, and $T_{Cr\text{-}Al\text{-}Opx}$ of 843–884°C, 935–980°C, and 933–962°C, respectively (Table 1). These temperature estimates are similar to those reported in previous studies of Tallante xenoliths using the same formulations (830–930°C [*Beccaluva et al*., 2004], 950–1020°C [*Shimizu et al*., 2008], and 960–1020°C [*Rampone et al*., 2010]).

To constrain the minimum pressure of spinel-garnet transition and that of plagioclase lherzolites, we applied the formulation of maximum stability of spinel lherzolite in the Cr-FCMAS system [*O'Neill*, 1981] and the anorthite (An) content of plagioclase in equilibrium with a lherzolite assemblage [*Borghini et al*., 2010, 2011], respectively (Figure 3). The uncertainty reported by the authors is ±0.15 GPa for the former and ±0.09 GPa for the latter geobarometer. The cluster-bearing xenoliths record minimum pressures of 1.83–1.91 GPa (~ 55–60 km), and the plagioclase-bearing ones originate at 0.62–0.73 (±0.09) GPa (~ 19–22 km) (Figure 3). The calculated stability field of plagioclase lherzolites is consistent with the 0.7–0.9 GPa pressure estimation for both the formation of intrusive veins [*Bianchini et al*., 2015; *Rampone et al*., 2010] and that of Al, Cr, and Ti zoning in pyroxenes [*Kogarko et al*., 2001].

8. Crystal Preferred Orientation

8.1. Data Acquisition, Treatment, and Calculations

We measured the crystal preferred orientation (CPO) of constituent phases by EBSD using the JEOL-JSM5600 scanning electron microscope at Géosciences Montpellier (Université de Montpellier, France) with acceleration voltage of 17 kV, working distance of 23 mm, 4 × 4 binning, and low gain. The HKL/Channel-5 software from Oxford Instruments was used for data acquisition, crystal orientation indexing, and data postprocessing. CPO maps of the xenoliths—covering most of the area of thin sections—were acquired in automatic mode with a variable step size of 20–100 μm so that step size is at least 5 times smaller than the average grain size of the recrystallized matrix grains. The indexing rate attained 57–91% for the samples. Offline data treatment was performed following the method of *Soustelle et al*. [2010] using the Channel-5 algorithms. The low amount of accessory phases (plagioclase, amphibole, and spinel) does not allow for the straightforward analysis of their orientation, hence, hereafter we focus on olivine and pyroxenes. Clusters and veins were treated as separated subsets wherever it was possible.

For oriented thin sections the CPO is shown in the structural reference frame with lineation and pole to the foliation at the E-W and N-S directions of the pole figures, respectively. For randomly cut thin sections, measured CPO were rotated into a common frame of reference, in which the maximum concentration of olivine [100] and [010] axes is parallel to the E-W and N-S directions of the pole figures, respectively. Note that this rotation does not affect neither the intensity nor the geometry of the CPO. To avoid overrepresentation of large crystals, we plot CPO for average grain orientations instead of individual measurements using the careware software package of David Mainprice (http://www.gm.univ-montp2.fr/PERSO/mainprice/W_data/CareWare_Unicef_Programs/).

The strength of the CPO is quantified by the *J* index, which is the volume-averaged integral of the squared orientation densities [*Bunge*, 1982]. This was derived from orientation distribution functions (ODF) calculated using the mean orientation of each grain with a "de la Vallée Poussin" kernel with a halfwidth of 10° using the MTEX toolbox in Matlab (https://mtex-toolbox.github.io/) [*Bachmann et al*., 2010; *Mainprice et al*., 2014]. The value of *J* index ranges from unity for a random fabric to infinity for a single crystal. Most natural peridotites show olivine *J* indices between 2 and 20, with a predominance of values ≤6 (>75% of the analyzed samples [cf. *Tommasi and Vauchez*, 2015]). For the calculation of pyroxene *J* indices, the veins and clusters have been removed from the peridotites.

To characterize the symmetry of olivine CPO, we calculated the BA index using the MTEX toolbox [*Mainprice et al*., 2014]. Based on the equation of BA index = $0.5 \times [2 - [P_{010}/(G_{010} + P_{010})] - [G_{100}/(G_{100} + P_{100})]]$, this parameter considers the point (*P*) and girdle (*G*) distribution of [010] and [100] crystallographic axes. For each axis these distributions are calculated from the orientation tensor and its three eigenvalues λ_1, λ_2, λ_3 (where

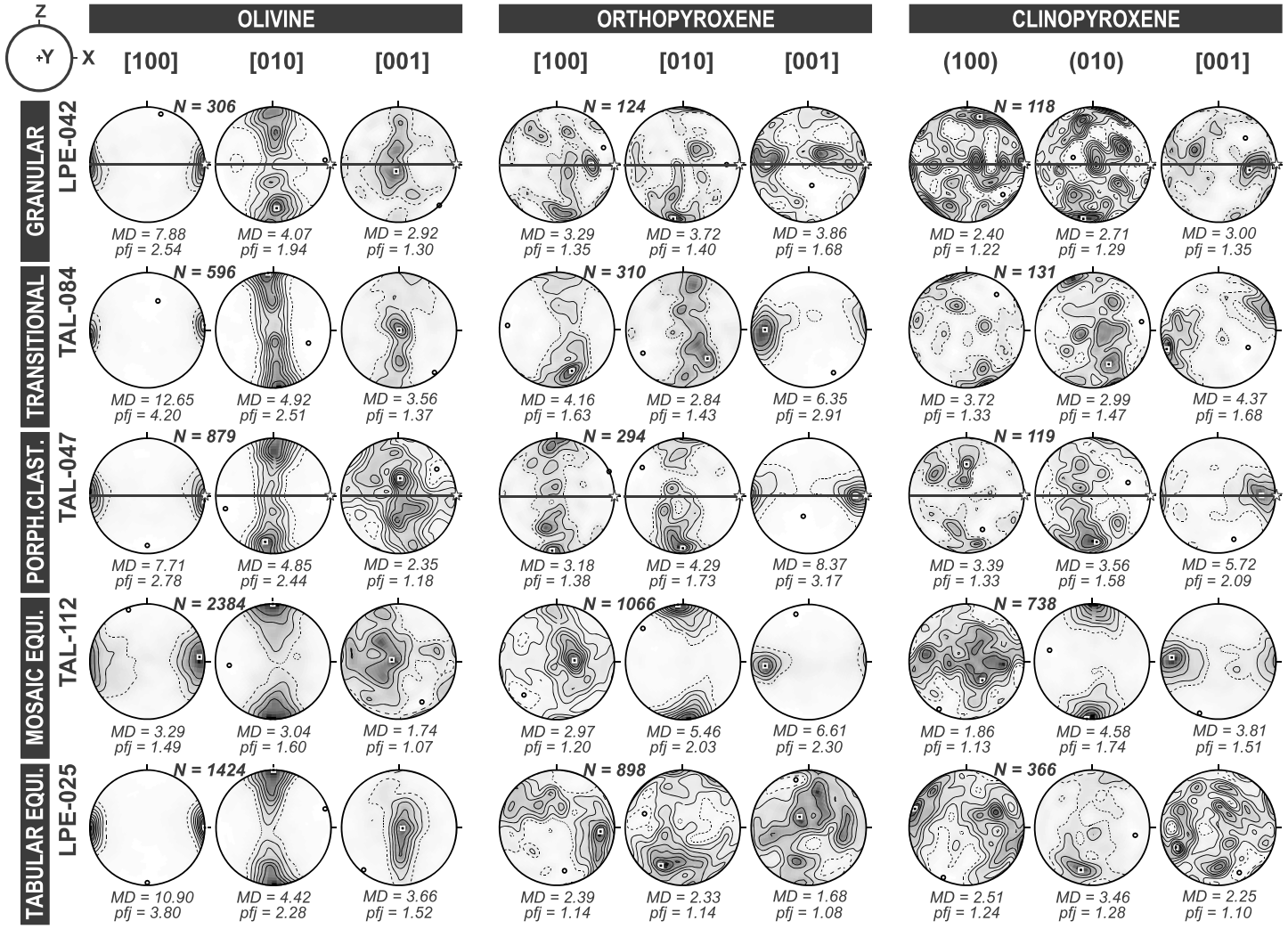

Figure 4. Lower hemisphere, equal area stereographic plots of the crystal preferred orientation (CPO) in representative SE Iberian mantle xenoliths from each textural group. For the full data set visit supporting information Figure S1. CPO are plotted using one average measurement per grain, contours at 0.5 multiples of a uniform distribution. In oriented thin sections of LPE-042 and TAL-047 the horizontal line denotes the foliation, and a white star corresponds to the lineation. The CPO in other xenoliths has been rotated in this reference frame in order to make the comparison possible. See text for further details on this rotation. N, number of measured grains; MD, maximum density; and pfj, scalar measure of the strength of the axis orientation in the pole figure.

$\lambda_1 \geq \lambda_2 \geq \lambda_3$ and $\lambda_1 + \lambda_2 + \lambda_3 = 1$ [*Vollmer*, 1990]) as $P = \lambda_1 - \lambda_2$ and $G = 2 \times (\lambda_2 - \lambda_3)$. For a perfect [010]-fiber CPO, the *P* and *G* values for [100] and [010] are 0, 1 and 1, 0, respectively, and the BA index is 0. In the other end-member case, a perfect [100]-fiber CPO the *P* and *G* values for [100] and [010] are 1, 0 and 0, 1, respectively; hence, the BA index is 1. In a perfect orthorhombic fabric, for both [100] and [010] *P* and *G* values are 1 and 0, respectively; thus, the BA index is 0.5. Note that this index only specifies CPO symmetry, but not the position of crystallographic axes with respect to structural elements in the rock (lineation and foliation).

Using MTEX we also estimate the average misorientation (due to accumulation of dislocations) within olivine grains by calculating the grain orientation spread (GOS), that is the average deviation of the orientation of a measurement point from the average orientation of the grain (cf. *Wright et al.* [2011] for a review). To evaluate remaining plastic strain in a xenolith, we average out GOS values of olivine weighted by the area of the grain to which the GOS value belongs, in order to avoid the overrepresentation of strain-free small grains.

8.2. Olivine and Pyroxenes in Peridotites

Tallante and Los Perez peridotites display well-developed olivine CPOs with variable intensities (Table 1, Figures 4, 5, and S1 in the supporting information). Equigranular xenoliths have weak olivine CPO (*J* index:

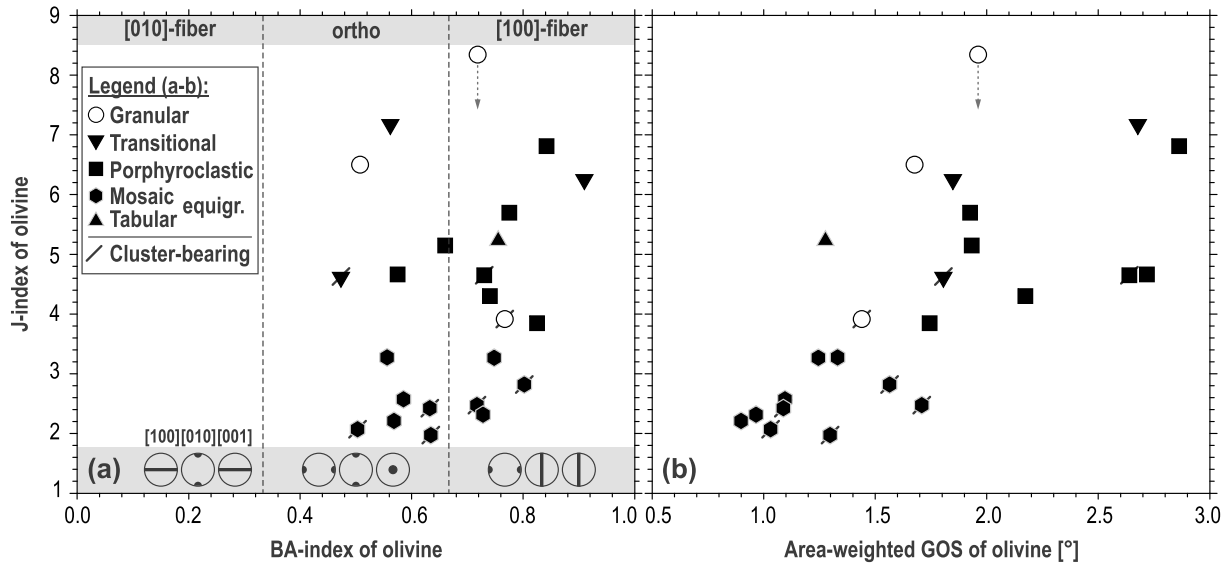

Figure 5. *J* index of olivine versus the (a) BA index of olivine and (b) the area-weighted grain orientation spread (GOS; in degrees) value of olivine in the different microstructures of the SE Iberian mantle xenoliths. Diagonal lines indicate cluster-bearing xenoliths. Dashed arrow specifies a particular sample for which the CPO strength might have been overestimated due to the coarse grain size. See text for details and Table 1 for data.

2.0–3.3), except for the tabular equigranular LPE-025, in which olivine is strongly oriented (*J* index: 5.2) (Figures 5a and 5b). Porphyroclastic, transitional, and granular xenoliths typically have stronger olivine CPO (*J* index in the range of 3.8–8.3), although the highest values may represent an overestimation of the CPO strength due to the coarse grain size (Figures 5a and 5b). The weak CPO of the equigranular xenoliths is associated with low intragranular misorientations, characterized by average grain orientation spread (GOS) values typically $<1.5°$, whereas the stronger CPO of the granular, transitional, and porphyroclastic xenoliths is accompanied with gradually increasing average intragranular misorientations at the sample scale (in the range of 1.4–2.9°) (Figure 5b).

Olivine CPO symmetry also varies, ranging from orthorhombic to [100]-fiber (BA indices from 0.47 to 0.91), with a minor predominance of [100]-fiber (14 xenoliths out of 24) (Figure 5a). These observations are consistent with the results of *Rampone et al*. [2010], who reported the same CPO types in Tallante mantle xenoliths. However, those authors observed the predominance of orthorhombic (010)[100] pattern with minor occurrence of [100]-fiber fabric. This slight discrepancy relative to the present data may be due to the limited number of grains (≤100) measured using universal stage in *Rampone et al*. [2010] that may have hindered the quantitative analyses of fabric types (i.e., calculation of BA indices and analyses of rotation axes of low-angle misorientations). There is no clear correlation between microstructural type and CPO symmetry, but the mosaic equigranular xenoliths show a tendency toward being orthorhombic, whereas the granular, transitional, and porphyroclastic xenoliths display more often [100]-fiber CPO (Figure 5a). Spinel-pyroxene clusters are observed in both CPO symmetry groups. As the BA indices indicate, olivine [100]-axes orientation is characterized by a strong point alignment in all xenoliths. In the oriented thin sections the maximum density of [100] is always subparallel to the lineation (Figure 4). In the [100]-fiber CPO symmetries, the dispersion of [010]-axes forms a girdle in a plane normal to the [100] maximum—with a maximum normal to the plane of the foliation in the oriented thin sections—and the [001]-axes either form a weak girdle parallel to the distribution of [010]-axes or are randomly oriented. In the xenoliths with orthorhombic CPO symmetry, the three crystallographic axes form point-like clusters at orthogonal directions, and in the oriented thin sections, [100]-, [010]-, and [001]-axes maximum concentrations are parallel to *X* (lineation), *Z* (normal to the foliation), and *Y* structural directions, respectively (Figure 4).

The CPO of orthopyroxene in most of the samples is more dispersed than that of olivine, but generally both minerals are correlated to each other (Figure 4 and supporting information Figure S1). Orthopyroxene CPO is characterized by strong alignment of [001]-axes subparallel to olivine [100], which is aligned with the stretching lineation in the oriented thin sections (Figure 4). The orthopyroxene [010]- and [100]-axes display weak

girdles normal to the maximum of [001], but often [010] has a weak maximum parallel to that of the olivine [010]—which is normal to the foliation in the oriented thin sections—and [100] is rather dispersed. Clear maxima of orthopyroxene [100] subparallel to olivine [010] are rarely observed. The tabular equigranular LPE-025 deviates from the above observations because the maxima of orthopyroxene [100]-, [010]-, and [001]-axes are subparallel to olivine [100], [010], and [001] axes, respectively (Figure 4). The *J* indices of orthopyroxene generally range from 2.2 to 5.3, except in the tabular equigranular LPE-025, where the orthopyroxene fabric is very weak (*J* index: 1.4) (Table 1). Orthopyroxene *J* indices are generally lower than those of olivine in the corresponding sample, except for the majority of mosaic equigranular xenoliths, where orthopyroxene fabric is significantly stronger than that of olivine (Table 1).

In most samples, clinopyroxenes exhibit rather weak CPOs, which in a few samples are almost random (LP08-12, LPE-025, and LPE-042) (Table 1, Figure 4, and supporting information Figure S1). When present, the clinopyroxene CPO is correlated with the olivine and orthopyroxene ones. Clinopyroxene [001] axes tend to be subparallel to olivine [100] and orthopyroxene [001] and are aligned parallel to the stretching lineation in the oriented thin sections (Figure 4). In samples with low clinopyroxene contents, the low number of measurements does not allow for the estimation of *J* indices. For the others, the clinopyroxene CPO strength shows the same pattern as the orthopyroxene one (Table 1). It is lower than that of olivine, except for the mosaic equigranular xenoliths.

8.3. Olivine and Pyroxenes in Veins and Clusters

The low modal amount of olivine, the limited number of grains, and the coarse grain size of constituent phases, particularly that of orthopyroxene, both in the orthopyroxenite veins and in the spinel-pyroxene clusters, do not allow for the statistical analyses of olivine and orthopyroxene CPO or the calculation of fabric strength in the veins and clusters. Nevertheless, orthopyroxene in the spinel-pyroxene clusters (Figure 2d), as well as olivine and orthopyroxene in the orthopyroxenite veins of the composite xenoliths (Figure 2g), shows identical CPO to olivine or orthopyroxene in the host peridotite. Olivine shows a strong point maximum of [100] and a girdle-like distribution of [010]- and [001]-axes, whereas orthopyroxene [001]-axes are aligned subparallel to olivine [100]-axes and orthopyroxene [100]- and [010]-axes are dispersed (Figure 2g).

9. Seismic Properties

In order to take into account the size of the crystals, seismic properties were computed using one orientation per pixel, instead of the average orientation of each grain in the thin section. The intrinsic seismic properties of mantle xenoliths were obtained by averaging the individual grain elastic constants tensor as a function of the CPO retrieved by EBSD measurements and modal composition [*Mainprice and Humbert*, 1994]. We used the Voigt-Reuss-Hill averaging method and single-crystal elastic constant tensors of olivine and pyroxenes at ambient conditions [*Abramson et al*., 1997; *Duffy and Vaughan*, 1988].

The seismic properties are very similar for all xenoliths regardless of the volcanic center, texture, and lithology, but the composite xenoliths have lower anisotropy (Table 1 and supporting information Figure S2). This observation is consistent with previous data indicating that pyroxene enrichment changes the density and reduces the seismic velocities of mantle rocks but has no particular impact on the fast *S* waves polarization direction resulting from *S* wave splitting, unless the original CPO is completely destroyed [*Tommasi et al*., 2004].

Considering the overall similarity of seismic properties of the SE Iberian mantle xenoliths, we calculated seismic properties for a bulk sample for each volcanic center (Figure 6). The bulk sample contains the orientation data of all xenoliths from a given volcanic center, which have been rotated in a common frame of reference as described in section 8.1. (*X* axis is parallel to the lineation, *XY* is the plane of foliation, and the *Z* axis is normal to foliation). Note that it is not possible to assess the original orientation of the foliation and lineation for the different xenoliths. Calculating average seismic properties supposing a common orientation of the foliation and lineation for all samples provides therefore an upper bound for the anisotropy. The assumption of a coherent orientation of the deformation over large distances (at the scale of the Fresnel zones) is nevertheless consistent with the large delay times obtained with *S* wave splitting measurements and the consistent and strong anisotropy of Pn waves (discussed later).

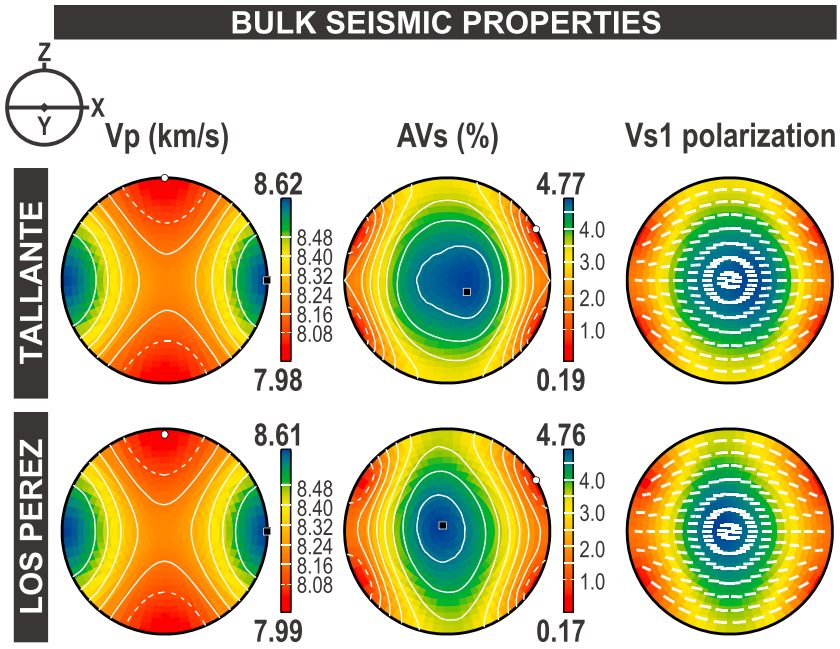

Figure 6. The calculated bulk seismic properties of Tallante and Los Perez xenoliths (12-12 samples) in lower hemisphere equal area stereographic projections. *Vp* is the 3-D distribution of *P* wave velocity (first column), AVs is 3-D distribution of the polarization anisotropy of *S* waves owing to *S* wave splitting (second column). V_{S1} polarization is a polarization plane of the fast split *S* wave as a function of orientation of the incoming wave relative to the structural framework of the sample; V_{S1} polarization is presented as superimposed on AVs (third column). The seismic properties of representative individual samples and the calculated bulk CPO are provided in supporting information Figures S2 and S3, respectively.

The calculated average olivine CPO is characterized by a [100]-fiber distribution (supporting information Figure S3) parallel to the flow direction (lineation). Figure 6 and supporting information Figure S2 show the three-dimensional distribution of the *P* waves velocity (*Vp*, km s^{-1}); the intensity of the *S* wave polarization anisotropy (AVs = $200 \cdot (V_{S1} - V_{S2})/(V_{S1} + V_{S2})$, in %, where V_{S1} and V_{S2} are, respectively, the velocities of the fast, S_1, and slow, S_2, polarized *S* wave); and the polarization direction of S_1 for representative xenoliths. Our calculations show that the propagation of *P* waves is fastest subparallel to the olivine [100]-axis maximum concentration (stretching lineation), and it is slowest parallel to the pole to the foliation (Table 1, Figure 6, and supporting information Figure S2). *S* wave splitting (AVs) is minimal for waves propagating within ~45° to the lineation in the plane containing the lineation and the normal to the foliation (plane *XZ*), and maximal for waves propagating near the perpendicular to the lineation in the foliation plane (Figure 6 and supporting information Figure S2). For all propagation directions, the fast split S_1 wave is polarized in a plane that contains the lineation and the propagation direction (Figure 6 and supporting information Figure S2), which corresponds to alignment of olivine [100]-axis.

10. Discussion

10.1. Microstructural Evolution of SE Iberian Mantle Xenoliths

SE Iberian mantle xenoliths with granular, transitional, and porphyroclastic microstructures show clear CPO (Figure 4), moderate to strong fabric strengths (Figure 5), and evidence of intracrystalline deformation of olivine and pyroxenes (Figures 2a and 2b), which are indicative of deformation by dislocation creep. The olivine, orthopyroxene, and clinopyroxene CPO are consistent with dominant activation of {0*kl*}[100] in olivine [e.g., *Tommasi et al*., 2000], of (100)[001] in orthopyroxene [e.g., *Soustelle et al*., 2010; *Frets et al*., 2014, and references therein], and of {110}[001] and (100)[001] slip systems in clinopyroxene [*Bascou et al*., 2002]. Overall, the CPOs in olivine and pyroxenes are consistent with deformation by dislocation glide creep at moderate temperature, low pressure, and fluid-absent conditions. The [100]-fiber fabric of olivine is characteristic of deformation regimes with a well-defined extension direction, such as simple shear, extrusion, or transtension [*Tommasi et al*., 1999].

The equigranular xenoliths have CPO patterns similar to those of granular and porphyroclastic rocks (Figure 4) but more dispersed. This nevertheless suggests the activation of the same olivine and pyroxene slip systems as in the coarser-grained peridotites. However, the equigranular xenoliths display near-equilibrium microstructures and lack subgrains and intragranular deformation microstructures (Figures 2c–2f; Figure 5b). This implies postkinematic annealing that restored the crystal structures but preserved the original CPO [e.g., *Tommasi et al*., 2008; *Vauchez and Garrido*, 2001]. Recovery of deformed grain interiors is often regarded as due to heating [e.g., *Borthwick et al*., 2014]; thus, the relatively low equilibrium temperatures obtained for the equigranular xenoliths (Table 1 and Figure 3) probably record cooling at shallow SCLM depths postdating annealing. *Rampone et al*. [2010] first interpreted the microstructures in transitional and equigranular xenoliths as produced by static annealing of porphyroclastic ones, related to extended stages of melt-rock interaction. The current microstructural data confirm and allow refining the model of melt-assisted annealing. The tabular equigranular xenolith LPE-025 shows indeed a unique microstructure characterized by orthopyroxene crystallographic axes that are weakly oriented (*J* index: 1.4) but distributed subparallel to those of olivine (*J* index: 5.2) (Table 1 and Figures 4 and 5). However, while the strong olivine fabric is consistent with the dominant activation of the olivine {0*kl*}[100] slip system, the orthopyroxene CPO cannot be accounted for by dislocation glide because only dislocations with [001] Burgers vectors have been observed in orthopyroxene [*Naze et al*., 1987]. Similar correlation between olivine and orthopyroxene CPOs has been reported in orthopyroxene-impregnated dunites from the Bay of Islands ophiolite [*Suhr*, 1993], as well as in ultramylonitic shear zones from the Othris ophiolite [*Dijkstra et al*., 2002] and the Ronda peridotite [*Hidas et al*., 2016]. In these studies, the unusual orthopyroxene CPO is interpreted as due to synkinematic melt or aqueous fluid-assisted oriented crystallization of orthopyroxene. We propose a similar interpretation for explaining the orthopyroxene CPO in the LPE-025 tabular equigranular xenolith.

The identical CPOs in the spinel-pyroxene clusters and in the host peridotite (Figure 2d) are consistent with prekinematic garnet breakdown corroborating the proposition of *Rampone et al*. [2010]. On the other hand, the similar olivine and pyroxene CPO in the orthopyroxenite veins and the peridotite wall rocks in composite xenoliths (Figure 2g) can be explained either by a deformation event that followed the formation of the veins or by oriented crystallization in synkinematic veins. We favor the latter possibility because the microstructure in composite xenoliths does not corroborate strong solid-state deformation. We therefore propose that the veins were formed during the waning stages of deformation. This interpretation is similar to that drawn by *Hidas et al*. [2015] to explain the orientation of constituent phases in gabbroic veins, which crosscut peridotites in the Ojén peridotite massif (Ronda peridotite).

We propose therefore that the postdeformational annealing of the shallowest portion of the SCLM (equigranular xenoliths) is likely due to melt-rock interaction, coeval to the formation of noritic veins that were dated as 6.8 ± 2.0 Ma by *Bianchini et al*. [2015] in other Tallante xenoliths. Furthermore, the homogeneity of olivine fabric, the overall consistency of olivine and pyroxene CPO, and the activation of the same dominant slip systems support that SE Iberian mantle xenoliths record a single deformation event. The oriented crystallization in the veins of the composite xenoliths constrained by the same stress field as the one recorded in the peridotites suggests that melt percolation is late to ductile deformation. Consequently, the ductile deformation event must be also late Neogene, which is significantly younger than proposed in previous studies [e.g., *Rampone et al*., 2010].

10.2. Seismic Anisotropy and Mantle Flow Beneath SE Iberia

In the western Mediterranean, the polarization of the fast split SKS wave (S_1) and the direction of the fastest refracted *P* waves (Pn) are both roughly parallel to the Betics orogenic fabric, rotating around the Gibraltar Arc [*Bokelmann et al*., 2011; *Buontempo et al*., 2008; *Diaz et al*., 2010; *Serrano et al*., 2005]. This supports that at least part of the measured shear waves splitting is due to the anisotropy of the lithospheric mantle [e.g., *Tommasi and Vauchez*, 2015]. In SE Iberia, the polarization of the fast shear wave S_1 trends mostly NE-SW [*Bokelmann et al*., 2011; *Buontempo et al*., 2008; *Diaz et al*., 2010], and the Pn anisotropy is fastest along ENE directions, coupled to normal uppermost mantle velocities (V_{Pn} of 8.1 km s^{-1} [*Díaz et al*., 2015; *Serrano et al*., 2005]). Measurements of splitting of SKS waves at the CART seismic station (Cartagena, Murcia) yield average fast polarization directions (Φ) of N69E $\pm 8°$ and delay times (δt) between the two split waves ranging from 1.52 ± 0.31 s [*Buontempo et al*., 2008] to 1.75 s [*Diaz et al*., 2010]; no error is reported in this study. Assuming that the <25 km thick crust in SE Iberia [*Mancilla et al*., 2015, and references therein]

contributes with maximum 0.3–0.5 s to the measured delay times [*Barruol and Mainprice*, 1993], the upper mantle contribution (lithosphere and asthenosphere) ranges between 1.0 and 1.2 ± 0.3 s. Three-dimensional gravity modeling combined with integrated heat flow and seismic tomography suggests that the base of the lithospheric mantle in the Cartagena area is at 60–70 km [*Torné et al*., 2000, Figure 9a] to 90–100 km [*Fullea et al*., 2010]. Analysis of teleseismic *P* residuals places the lithosphere-asthenosphere boundary in the easternmost inner Betics at depths of ~ 80 km [*Plomerová et al*., 1993]. Finally, receiver function analysis implies a lithosphere-asthenosphere boundary at 50 km depth [*Mancilla et al*., 2015]. Altogether, these observations indicate that the current total thickness of the mantle lithosphere in the SE Iberian margin ranges between 40 and 80 km.

The delay times between split SKS waves are highly dependent on the dip of the foliation and the direction of the lineation in the upper mantle [e.g., *Mainprice and Silver*, 1993; *Vauchez et al*., 2012, and references therein]. The strong anisotropy and the coherent orientation of the fast split waves and fastest Pn waves indicate that anisotropy in the SE Iberian lithospheric mantle must be vertically coherent starting from just below the Moho [e.g., *Buontempo et al*., 2008]. Together with the predominance of [100]-fiber fabrics in the SE Iberian mantle xenoliths, this observation unambiguously constrains the direction of active or frozen mantle flow in the upper mantle to be horizontal and parallel to the to the trend of the belt (Figure 6).

To further constrain the orientation of the SCLM structures, we calculated theoretical SKS delay times based on the average seismic properties of the SE Iberian mantle xenoliths (Figure 6) assuming all xenoliths have a similarly oriented tectonic fabric. Depending on the range of estimated crustal contribution, a geometry with a shallowly dipping foliation and subhorizontal lineation parallel to the trend of the Betics belt would require an anisotropic upper mantle 147–176 km thick to account for delay times observed at the CART station. For a steeply dipping foliation and subhorizontal lineation an anisotropic mantle layer 103–123 km thick is needed.

Considering that the igneous veins and the equigranular xenoliths—which reduce the seismic anisotropies (Table 1)—display typical equilibration conditions <40 km depth (dominantly <1000°C, Table 1; 0.7–0.9 GPa [*Bianchini et al*., 2015]), hence can influence maximum the uppermost 13–18 km of the lithospheric mantle (cf. Moho depth in *Mancilla et al*. [2015]), we may suppose that most of the SCLM beneath the study area is composed by the more anisotropic porphyroclastic and granular peridotites (Table 1). If we assume that the major part of the SCLM beneath SE Iberia is characterized by coarser-grained microstructures and lack igneous veins, the measured seismic properties at the CART station may be accounted for by an anisotropic mantle layer either 81–96 km thick (shallowly dipping foliation and subhorizontal lineation) or 65–78 km thick (steeply dipping foliation and subhorizontal lineation). In contrast, vertical lineations in the SCLM [e.g., *Julià et al*., 2005; *Shimizu et al*., 2004, and references therein] would result in negligible splitting for vertically propagating SKS waves, hence would require at least 4000 km of anisotropic layer with vertical foliation and lineation to explain seismic anisotropy data recorded at the surface.

Considering together the fast shear wave polarizations, Pn direction of fast propagation at the CART seismic station [*Buontempo et al*., 2008; *Díaz et al*., 2015; *Serrano et al*., 2005], the total thickness of the mantle lithosphere beneath the region, and the dominant [100]-fiber CPO symmetry of the studied xenoliths (Figures 4 and 5), we can conclude that the olivine [100]-axes and, hence, the frozen flow directions in the lithospheric mantle are dominantly subhorizontal and oriented in a direction close to the tectonic trend of the Betics. A horizontal SCLM foliation with a belt-parallel lineation in the lithospheric mantle requires significant contribution from the asthenosphere to the seismic anisotropy data, and this geometry may only explain the measurements if we assume similar belt-parallel flow directions both in the lithosphere and in the upper part of the asthenosphere. This is, however, not consistent with the tectonic fabric described in the crust of the Betics [e.g., *Booth-Rea et al*., 2005, 2007; *Platt et al*., 2013, and references therein], and it would imply crust-mantle decoupling. Moreover, such a fabric in the lithospheric mantle would involve thrusting in a direction parallel to the belt, a process that is difficult to integrate in the current geodynamic models of the Betics [e.g., *Platt et al*., 2013, and references therein]. In contrast, the strong delay times observed at the CART seismic station may be produced in the lithospheric mantle (with a minor contribution of the asthenosphere) if the SKS waves propagate within the foliation but at high angle to the lineation, that is, if the foliation is vertical and the lineation is subhorizontal, and subparallel to the Iberian margin (Figure 7). Such a mantle structure implies a strong strike-slip component of flow parallel to the belt as proposed by *Vauchez and Nicolas* [1991]. This

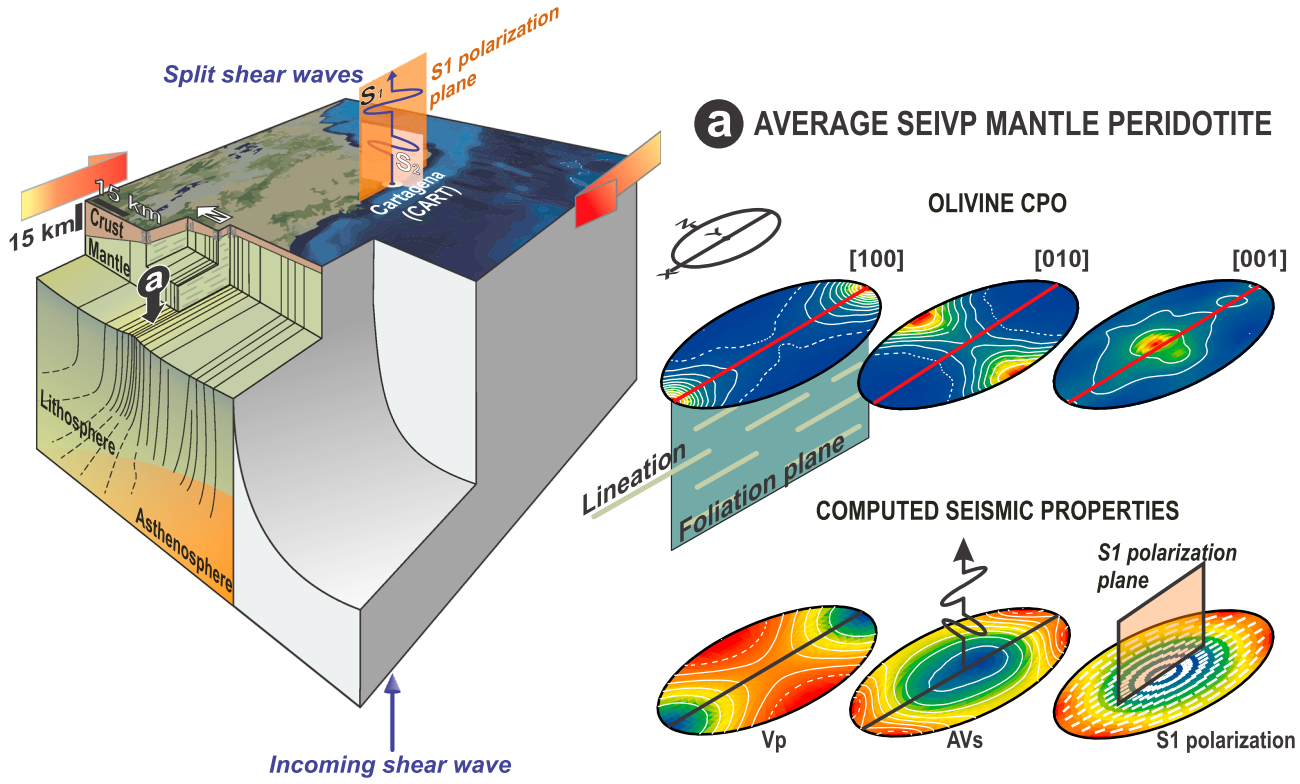

Figure 7. Conceptual model for the subcontinental lithospheric mantle beneath SE Iberia (modified after *Vauchez et al*. [2012]). The structures are reconstructed to explain seismic anisotropies measured at the Cartagena (CART) station assuming a vertically incident polarized SKS wave that propagates through the studied vertically foliated and horizontally lineated subcontinental lithospheric mantle section (see text for details). In (a) we present the average olivine CPO of the SE Iberian mantle xenoliths that resulted from the preeruptive transtensive deformation stress field (orange arrows), as well as we show the calculated 3-D seismic properties of the mantle rocks in the same structural reference frame. Olivine CPO has [100]-axes subparallel to the lineation and the maxima of [010]- and [001]-axes close to the normal to the foliation plane, and orthogonal to the lineation in the foliation plane, respectively (cf. supporting information Figure S3). The *Vp* diagram shows the highest *P* wave velocity parallel to [100]-axis; the AVs (δVs) diagram shows the velocity difference between the fast and slow split *S* waves for all propagation directions; the maximum birefringence is for *S* waves propagating in a direction normal to the lineation, i.e., with a subvertical incidence in the case shown in the main figure. The S1 polarization diagram shows the orientation of the plane in which the fast *S* wave is polarized; this plane is consistently defined by the fast *S* wave propagation direction.

mantle geometry has been indeed inferred based on seismic anisotropy data in many other mountain belts worldwide [*Silver*, 1996; *Vauchez et al*., 2012].

10.3. Implications for Mantle Flow and Neogene Geodynamics of SE Iberia

The westernmost Mediterranean provides various opportunities to study rocks of the SCLM. These localities include mantle xenoliths brought to the surface by late Neogene alkali basalts, as well as the protracted record of the largest outcrops of the SCLM in the Ronda and Beni Bousera peridotite massifs (Figure 1).

The olivine and orthopyroxene CPOs of SE Iberian xenoliths differ from those of the Ronda massif and indicate ductile deformation under a different tectonic regime. The Ronda peridotite records simple shear deformation under variable pressure and temperature conditions and displays dominantly axial-[010] and orthorhombic olivine CPO [*Soustelle et al*., 2009; *Vauchez and Garrido*, 2001]. The olivine CPO of SE Iberian mantle xenoliths shows a predominance of [100]-fiber patterns, which are characteristic of deformation at high temperature under simple shear or transtension [*Tommasi et al*., 1999].

The postdeformation annealing of the shallowest portion of the SCLM was possibly enhanced by melt-rock interaction. Available dating of the orthopyroxenite veins [*Bianchini et al*., 2015] suggests that the deformation event that produced the CPO of the SE Iberian mantle xenoliths ended around 6.8 ± 2.0 Ma ago. In western Betics-Rif orogenic peridotites the ductile deformation is minimum Late Oligocene-Early Miocene [*Garrido et al*., 2011] based on the 24 ± 3 Ma Lu-Hf cooling ages in clinopyroxene-garnet pairs in garnet

pyroxenites, with closure temperatures at ~ 800°C [*Pearson and Nowell*, 2004], which is at odds to the relatively young ages for the deformation recorded in SE Iberian mantle xenoliths. These age differences show that while Ronda peridotite massif records ductile deformation shortly before the collision of the Alborán wedge with the paleo-Iberian and African margin [*Garrido et al*., 2011; *Hidas et al*., 2013; *Precigout et al*., 2013], the SE Iberian xenoliths record ductile mantle deformation coeval with late Neogene slab rollback and tearing of the subducted Iberian paleomargin [*Booth-Rea et al*., 2015; *Mancilla et al*., 2015].

The deformation event recorded in the SE Iberian mantle xenoliths postdates, therefore, the ductile thinning of the SCLM, as well as the initiation of lower crustal anatexis in SE Iberia recorded in crustal xenoliths from late Miocene, calc-alkaline volcanoes [e.g., *Acosta-Vigil et al*., 2010, and references therein] and dated between 9.7 and 8.1 Ma [*Cesare et al*., 2003]. *Alvarez-Valero and Kriegsman* [2007] have argued that crustal anatexis—triggered by basaltic magma underplating—occurred in the late Miocene. This time span also coincides with the change from subduction-related to intraplate-type volcanism (6.3–4.8 Myr) in the SE Iberian margin, which is largely synchronous with the decompression associated with the Messinian salinity crisis [*Duggen et al*., 2003, 2004, and references therein]. The end of the process coincides with Pliocene exhumation of the eastern Betics and the eastern Iberian margin that could have been driven by a late heating event due to asthenospheric upwelling related to continental edge delamination [*Duggen et al*., 2005] during the post-Miocene [*Janssen et al*., 1993]. Widespread magmatic activity during the middle Miocene to Pliocene in SE Iberia coincides with areas where the base of the lithosphere is shallow (<60 km [*Mancilla et al*., 2015]). These observations indicate close relationships between lithosphere thinning, heating, crustal anatexis, magmatism, and exhumation in the late Miocene and Pliocene in SE Iberia.

The Neogene transtensional deformation regime with a dominant strike-slip component, as inferred combining microstructures and CPO of the mantle xenoliths with seismic anisotropy data, is consistent with late Miocene crustal extension and associated subsidence in SE Iberia [*Booth-Rea et al*., 2007, and references therein]. Moreover, extensional core-complex-type domes elongated in the direction of extension like those described in the Betics [*Martinez-Martinez et al*., 2002] are typical of transtensional tectonic regimes as supported by 3-D thermomechanical modeling for core complexes in the Hellenic arc [*Le Pourhiet et al*., 2012]. However, late Miocene to present-day crustal structures in the eastern Betics and in most of the Alborán domain are dominantly compressional or strike-slip, including large-scale open folds, reverse, and transcurrent faults [*Booth-Rea et al*., 2007; *Giaconia et al*., 2015, and references therein] in agreement with the current NW-SE convergence between Nubia and Eurasia.

Seismic observations suggest the existence of an east to southeast dipping high-velocity body in the upper mantle below the Gibraltar arc, interpreted as subducted oceanic and/or delaminated continental lithosphere [*Spakman and Wortel*, 2004, and references therein]. A growing body of evidence supports the hypothesis that both subduction rollback and tearing beneath the continental margins may have contributed to the formation and development of the Gibraltar arc [*Booth-Rea et al*., 2007; *Duggen et al*., 2005; *Mancilla et al*., 2015, and references therein]. The combination of Miocene westward slab retreat forming the Alborán Basin and late Miocene rupture of the Iberian margin may account for some features observed in the eastern inner Betics mantle xenoliths.

Based on the coherence between the crustal fabric and fast polarization of SKS waves, *Vauchez and Nicolas* [1991] suggested that in many collisional belts the mantle flow is dominantly orogen parallel. In SE Iberia it is unlikely that belt-parallel mantle flow results from the NW-SE convergence of Nubia and Iberia, which has influenced the tectonics of the Betics mostly since the late Tortonian [e.g., *Giaconia et al*., 2015, and references therein]. An alternative is that the mantle fabric producing the measured belt-parallel anisotropy resulted from Miocene slab tearing and rollback processes. The fast W-SW slab retreat in the Miocene may have induced a large strike-slip deformation in the mantle at the edge of the Iberian and Nubian plates, generating a strong belt-parallel anisotropy on both margins. Tearing of the Iberian margin mantle may have caused lateral westward inflow of hot and extended lithospheric mantle of Alborán provenance under the detached margins flowing parallel to Iberia [*Mancilla et al*., 2015]. An extensional component associated with this strike-slip flow may account for the heating, crustal anatexis, shift of magmatism, crustal extension, and exhumation of the eastern Betics in the late Miocene to Pliocene.

Despite the post-Tortonian NW-SE convergence, we cannot discard that reactivation of deformation structures inherited from previous tectonic events in the SE Iberian mantle may have induced anisotropic viscosity

and controlled the recent belt-parallel mantle flow during slab tearing and rollback processes [*Tommasi et al*., 2009]. The presence of inherited middle to late Miocene, or even older, fabrics in the shallow mantle beneath SE Iberia may continue governing some tectonic processes. Earthquake moment tensors indicate deep strike-slip faulting in SE Iberia coherent with motion in a NE-SW trending left-lateral shear zone [*Stich et al*., 2006], processes that are in principle incompatible with the general NW-SE plate convergence between Africa and Iberia. This deformation may, however, be explained if a CPO-induced mechanical anisotropy in the SE Iberian lithospheric mantle is considered since the latter will favor shearing parallel to the preexisting olivine CPO in the SCLM [*Tommasi and Vauchez*, 2015; *Tommasi et al*., 2009].

11. Conclusions

We studied mantle xenoliths, including spinel ± plagioclase-bearing peridotites and orthopyroxenite veins in composite rocks, outcropped by Pliocene alkali basalts in SE Iberia. This xenolith suite provides a snapshot of the structure and composition of the lithospheric mantle beneath the NE termination of the Alborán arc system in the western Mediterranean. The peridotites show dominantly [100]-fiber olivine CPO, compatible with deformation under a transtensional tectonic regime. Orthopyroxene CPO is generally coherent with the olivine one. In one sample, we observe, however, a subparallel distribution of olivine and orthopyroxene crystallographic axes, which we interpret as due to synkinematic oriented crystallization of the orthopyroxene. Pyroxenes in pyroxenite veins of composite xenoliths show identical CPO to those in the host peridotites, which implies oriented crystallization controlled by the same stress field. A large number of mantle xenoliths, in particular those characterized by the lower equilibration temperatures, show annealed microstructures, but they display essentially the same CPO as the coarser-grained and more deformed porphyroclastic peridotites. This suggests postdeformational annealing of the shallowest portion of the SCLM possibly due to melt-rock interaction. Available dating of orthopyroxenite veins supports that melt percolation and melt-enhanced recovery are late Neogene in age. The oriented crystallization in the veins of composite xenoliths suggests that the peak of ductile deformation slightly predates this recovery, demonstrating that ductile fabrics were also developed sometime in the late Miocene.

The polarization of the fast split SKS waves and highest Pn velocity oriented ~ N70°E in SE Iberia may be explained by a lithospheric mantle fabric with olivine [100]-axes subhorizontal trending ENE. Considering the limited mantle lithosphere thickness (40–80 km) in the region, the SKS delay times in SE Iberia can only be accounted by deformation in the lithospheric mantle if the foliation is steeply dipping and the lineation is subhorizontal. This geometry of the lithospheric mantle peridotite fabric implies active or frozen mantle flow with a dominantly ENE-WSW strike-slip component subparallel to the south Iberian paleomargin.

Analysis of seismic anisotropy data in the light of the seismic properties of the SE Iberian mantle xenoliths points, therefore, to mantle lithospheric thinning accommodated by a transtensional regime with a dominant strike-slip component in the late Neogene, possibly during WSW tearing of the subducted Iberian margin lithosphere. The existence of strike-slip inherited mantle fabrics may continue governing some deep processes in SE Iberia via the mechanical anisotropy it induces in the SCLM and coupling between mantle and crustal deformations.

Acknowledgments

We are grateful to R. Reyes González for sample and thin section preparation, to A. Caballero and M.J. Roman Alpiste for drawing Figure 7, and to F. Barou for his assistance during EBSD-SEM analyses. We acknowledge the constructive comments of the Associate Editor Djordje Grujic and two reviewers, Whitney M. Behr and Sarah Brownlee, as well as the careful editorial work of John W. Geissman. This work was supported by the International Lithosphere Program (CC4-MEDYNA), the "Spanish Ministry of Economic and Competitiveness" (MINECO) grants CGL2013-42349 and PCIN-2015-053, and the "Junta de Andalucía" research group RNM-131. We acknowledge MINECO funding of the "Juan de la Cierva" Postdoctoral Fellowship (FPDI-2013-16253) to K.H. and the "Ramón y Cajal" Fellowship (RYC-2012-11314) to C.M. The CSIC is acknowledged for funding two JAE-Predoc fellowships to Z.K. and M.I.V.R. Fellowships and grants leading to this research have been (co)funded by the European Social Fund and the European Regional Development Fund. The data used in this paper are listed in the references, tables, and supporting information. The raw EBSD data files are available from the corresponding author upon request.

References

Abramson, E. H., J. M. Brown, L. J. Slutsky, and J. Zaug (1997), The elastic constants of San Carlos olivine to 17 GPa, *J. Geophys. Res.*, *102*, 12,253–12,263, doi:10.1029/97JB00682.

Acosta-Vigil, A., I. Buick, J. Hermann, B. Cesare, D. Rubatto, D. London, and G. B. Morgan (2010), Mechanisms of crustal anatexis: A geochemical study of partially melted metapelitic enclaves and host dacite, SE Spain, *J. Petrol.*, *51*(4), 785–821.

Alvarez-Valero, A. M., and L. M. Kriegsman (2007), Crustal thinning and mafic underplating beneath the Neogene Volcanic Province (Betic Cordillera, SE Spain): Evidence from crustal xenoliths, *Terra Nova*, *19*(4), 266–271.

Bachmann, F., R. Hielscher, and H. Schaeben (2010), Texture analysis with MTEX—Free and open source software toolbox, *Solid State Phenom.*, *160*, 63–68.

Barruol, G., and D. Mainprice (1993), A quantitative evaluation of the contribution of crustal rocks to the shear-wave splitting of teleseismic SKS waves, *Phys. Earth Planet. Inter.*, *78*(3), 281–300.

Bascou, J., A. Tommasi, and D. Mainprice (2002), Plastic deformation and development of clinopyroxene lattice preferred orientations in eclogites, *J. Struct. Geol.*, *24*(8), 1357–1368.

Beccaluva, L., G. Bianchini, C. Bonadiman, F. Siena, and C. Vaccaro (2004), Coexisting anorogenic and subduction-related metasomatism in mantle xenoliths from the Betic Cordillera (southern Spain), *Lithos*, *75*(1–2), 67–87.

Bianchini, G., L. Beccaluva, G. M. Nowell, D. G. Pearson, and F. Siena (2011), Mantle xenoliths from Tallante (Betic Cordillera): Insights into the multi-stage evolution of the south Iberian lithosphere, *Lithos*, *124*(3–4), 308–318.

Bianchini, G., R. Braga, A. Langone, C. Natali, and M. Tiepolo (2015), Metasedimentary and igneous xenoliths from Tallante (Betic Cordillera, Spain): Inferences on crust-mantle interactions and clues for post-collisional volcanism magma sources, *Lithos*, *220–223*, 191–199.

Bokelmann, G., E. Maufroy, L. Buontempo, J. Morales, and G. Barruol (2011), Testing oceanic subduction and convective removal models for the Gibraltar arc: Seismological constraints from dispersion and anisotropy, *Tectonophysics*, *502*(1–2), 28–37.

Booth-Rea, G., J. M. Azañón, J. M. Martínez-Martínez, O. Vidal, and V. García-Dueñas (2005), Contrasting structural and P-T evolution of tectonic units in the southeastern Betics: Key for understanding the exhumation of the Alboran Domain HP/LT crustal rocks (western Mediterranean), *Tectonics*, *24*, TC2009, doi:10.1029/2004TC001640.

Booth-Rea, G., C. R. Ranero, J. M. Martinez-Martinez, and I. Grevemeyer (2007), Crustal types and Tertiary tectonic evolution of the Alboran Sea, western Mediterranean, *Geochem. Geophys. Geosyst.*, *8*, Q10005, doi:10.1029/2007GC001639.

Booth-Rea, G., J. M. Martínez-Martínez, and F. Giaconia (2015), Continental subduction, intracrustal shortening, and coeval upper-crustal extension: P-T evolution of subducted south Iberian paleomargin metapelites (Betics, SE Spain), *Tectonophysics*, *663*, 122–139.

Borghini, G., P. Fumagalli, and E. Rampone (2010), The stability of plagioclase in the upper mantle: Subsolidus experiments on fertile and depleted lherzolite, *J. Petrol.*, *51*(1–2), 229–254.

Borghini, G., P. Fumagalli, and E. Rampone (2011), The geobarometric significance of plagioclase in mantle peridotites: A link between nature and experiments, *Lithos*, *126*(1–2), 42–53.

Borthwick, V. E., S. Piazolo, L. Evans, A. Griera, and P. D. Bons (2014), What happens to deformed rocks after deformation? A refined model for recovery based on numerical simulations, *Geol. Soc. London Spec. Publ.*, *394*(1), 215–234.

Brey, G. P., and T. Köhler (1990), Geothermobarometry in four-phase lherzolites. II. New thermobarometers, and practical assessment of existing thermobarometers, *J. Petrol.*, *31*(6), 1353–1378.

Bunge, H. J. (1982), *Texture Analysis in Materials Sciences*, 593 pp., Butterworth, London.

Buontempo, L., G. H. R. Bokelmann, G. Barruol, and J. Morales (2008), Seismic anisotropy beneath southern Iberia from SKS splitting, *Earth Planet. Sci. Lett.*, *273*(3–4), 237–250.

Calvert, A., E. Sandvol, D. Seber, M. Barazangi, S. Roecker, T. Mourabit, F. Vidal, G. Alguacil, and N. Jabour (2000), Geodynamic evolution of the lithosphere and upper mantle beneath the Alboran region of the western Mediterranean: Constraints from travel time tomography, *J. Geophys. Res.*, *105*, 10,871–10,898, doi:10.1029/2000JB900024.

Capedri, S., G. Venturelli, E. Salvioli-Mariani, A. J. Crawford, and M. Barbieri (1989), Upper-mantle xenoliths and megacrysts in an alkali basalt from Tallante, south-eastern Spain, *Eur. J. Mineral.*, *1*(5), 685–699.

Cebriá, J. M., J. López-Ruiz, J. Carmona, and M. Doblas (2009), Quantitative petrogenetic constraints on the Pliocene alkali basaltic volcanism of the SE Spain Volcanic Province, *J. Volcanol. Geotherm. Res.*, *185*(3), 172–180.

Cesare, B., M. T. Gómez-Pugnaire, and D. Rubatto (2003), Residence time of S-type anatectic magmas beneath the Neogene Volcanic Province of SE Spain: A zircon and monazite SHRIMP study, *Contrib. Mineral. Petrol.*, *146*(1), 28–43.

Comas, M. C., J. P. Platt, J. I. Soto, and A. B. Watts (1999), The origin and tectonic history of the Alboran Basin: Insights from Leg 161 results, in *Proceedings of the Ocean Drilling Program, Scientific Results*, edited by R. Zahn, M. C. Comas, and A. Klaus, pp. 555–580, Ocean Drill. Program, College Station, Tex.

Diaz, J., J. Gallart, A. Villaseñor, F. Mancilla, A. Pazos, D. Córdoba, J. A. Pulgar, P. Ibarra, and M. Harnafi (2010), Mantle dynamics beneath the Gibraltar Arc (western Mediterranean) from shear-wave splitting measurements on a dense seismic array, *Geophys. Res. Lett.*, *37*, L18304, doi:10.1029/2010GL044201.

Díaz, J., J. Gallart, I. Morais, G. Silveira, D. Pedreira, J. A. Pulgar, N. A. Dias, M. Ruiz, and J. M. González-Cortina (2015), From the Bay of Biscay to the High Atlas: Completing the anisotropic characterization of the upper mantle beneath the westernmost Mediterranean region, *Tectonophysics*, *663*, 192–202.

Dijkstra, A. H., M. R. Drury, R. L. M. Vissers, and J. Newman (2002), On the role of melt-rock reaction in mantle shear zone formation in the Othris peridotite massif (Greece), *J. Struct. Geol.*, *24*(9), 1431–1450.

Doblas, M., J. López-Ruiz, and J.-M. Cebriá (2007), Cenozoic evolution of the Alboran Domain: A review of the tectonomagmatic models, *Geol. Soc. Am. Spec. Pap.*, *418*, 303–320.

Duffy, T. S., and M. T. Vaughan (1988), Elasticity of enstatite and its relationship to crystal structure, *J. Geophys. Res.*, *93*, 383–391, doi:10.1029/JB093iB01p00383.

Duggen, S., K. Hoernle, P. van den Bogaard, L. Rupke, and J. P. Morgan (2003), Deep roots of the Messinian salinity crisis, *Nature*, *422*(6932), 602–606.

Duggen, S., K. Hoernle, P. van den Bogaard, and C. Harris (2004), Magmatic evolution of the Alboran region: The role of subduction in forming the western Mediterranean and causing the Messinian salinity crisis, *Earth Planet. Sci. Lett.*, *218*(1–2), 91–108.

Duggen, S., K. Hoernle, P. Van den Bogaard, and D. Garbe-Schonberg (2005), Post-collisional transition from subduction- to intraplate-type magmatism in the westernmost Mediterranean: Evidence for continental-edge delamination of subcontinental lithosphere, *J. Petrol.*, *46*(6), 1155–1201.

Duggen, S., K. Hoernle, A. Kluegel, J. Geldmacher, M. Thirlwall, F. Hauff, D. Lowry, and N. Oates (2008), Geochemical zonation of the Miocene Alborán Basin volcanism (westernmost Mediterranean): Geodynamic implications, *Contrib. Mineral. Petrol.*, *156*(5), 577–593.

England, P., and P. Molnar (1990), Surface uplift, uplift of rocks, and exhumation of rocks, *Geology*, *18*(12), 1173–1177.

Frets, E. C., A. Tommasi, C. J. Garrido, A. Vauchez, D. Mainprice, K. Targuisti, and I. Amri (2014), The Beni Bousera peridotite (Rif Belt, Morocco): An oblique-slip low-angle shear zone thinning the subcontinental mantle lithosphere, *J. Petrol.*, *55*(2), 283–313.

Fullea, J., M. Fernandez, J. C. Afonso, J. Verges, and H. Zeyen (2010), The structure and evolution of the lithosphere-asthenosphere boundary beneath the Atlantic-Mediterranean transition region, *Lithos*, *120*(1–2), 74–95.

Garrido, C. J., F. Gueydan, G. Booth-Rea, J. Precigout, K. Hidas, J. A. Padron-Navarta, and C. Marchesi (2011), Garnet lherzolite and garnet-spinel mylonite in the Ronda peridotite: Vestiges of Oligocene backarc mantle lithospheric extension in the western Mediterranean, *Geology*, *39*(10), 927–930.

Giaconia, F., et al. (2015), Compressional tectonic inversion of the Algero-Balearic basin: Latemost Miocene to present oblique convergence at the Palomares margin (western Mediterranean), *Tectonics*, *34*, 1516–1543, doi:10.1002/2015TC003861.

Hidas, K., G. Booth-Rea, C. J. Garrido, J. M. Martínez-Martínez, J. A. Padrón-Navarta, Z. Konc, F. Giaconia, E. Frets, and C. Marchesi (2013), Backarc basin inversion and subcontinental mantle emplacement in the crust: Kilometre-scale folding and shearing at the base of the proto-Alborán lithospheric mantle (Betic Cordillera, southern Spain), *J. Geol. Soc.*, *170*(1), 47–55.

Hidas, K., M. I. Varas-Reus, C. J. Garrido, C. Marchesi, A. Acosta-Vigil, J. A. Padrón-Navarta, K. Targuisti, and Z. Konc (2015), Hyperextension of continental to oceanic-like lithosphere: The record of late gabbros in the shallow subcontinental lithospheric mantle of the westernmost Mediterranean, *Tectonophysics*, *650*, 65–79.

Hidas, K., A. Tommasi, C. J. Garrido, J. A. Padrón-Navarta, D. Mainprice, A. Vauchez, F. Barou, and C. Marchesi (2016), Fluid-assisted strain localization in the shallow subcontinental lithospheric mantle, *Lithos*, *262*, 636–650.

Hoernle, K., P. Van den Bogaard, S. Duggen, B. Mocek, and D. Garbe-Schonberg (1999), Evidence for Miocene subduction beneath the Alboran Sea: $^{40}Ar/^{39}Ar$ dating and geochemistry of volcanic rocks from holes 977A and 978A, in *Proceedings of the Ocean Drilling Program, Scientific Results*, edited by R. Zahn, M. C. Comas, and A. Klaus, pp. 357–373, Ocean Drill. Program, College Station, Tex.

Janssen, M. E., M. Torné, S. Cloetingh, and E. Banda (1993), Pliocene uplift of the eastern Iberian margin—Inferences from quantitative modeling of the Valencia trough, *Earth Planet. Sci. Lett.*, *119*(4), 585–597.

Jolivet, L., and C. Faccenna (2000), Mediterranean extension and the Africa-Eurasia collision, *Tectonics*, *19*, 1095–1106, doi:10.1029/2000TC900018.

Julià, J., F. L. Mancilla, and J. Morales (2005), Seismic signature of intracrustal magmatic intrusions in the Eastern Betics (Internal Zone), SE Iberia, *Geophys. Res. Lett.*, *32*, L16304, doi:10.1029/2005GL023274.

Kogarko, L. N., I. D. Ryabchikov, G. P. Brey, S. F. Santin, and H. Pacheco (2001), Mantle rocks uplifted to crustal levels: Diffusion profiles in minerals of spinel-plagioclase lherzolites from Tallante, Spain, *Geochem. Int.*, *39*(4), 311–326.

Konc, Z. (2013), Structure and composition of the subcontinental lithospheric mantle in convergent settings—Insights from mantle xenoliths hosted in alkaline magmatism, PhD thesis, 209 pp., Univ. de Granada, Granada, Spain.

Le Pourhiet, L., B. Huet, D. A. May, L. Labrousse, and L. Jolivet (2012), Kinematic interpretation of the 3D shapes of metamorphic core complexes, *Geochem. Geophys. Geosyst.*, *13*, Q09002, doi:10.1029/2012GC004271.

Lonergan, L., and N. White (1997), Origin of the Betic-Rif mountain belt, *Tectonics*, *16*, 504–522, doi:10.1029/96TC03937.

Mainprice, D., and M. Humbert (1994), Methods of calculating petrophysical properties from lattice preferred orientation data, *Surv. Geophys.*, *15*(5), 575–592.

Mainprice, D., and P. G. Silver (1993), Interpretation of SkS-waves using samples from the subcontinental lithosphere, *Phys. Earth Planet. Inter.*, *78*(3-4), 257–280.

Mainprice, D., F. Bachmann, R. Hielscher, and H. Schaeben (2014), Descriptive tools for the analysis of texture projects with large datasets using MTEX: Strength, symmetry and components, *Geol. Soc. London Spec. Publ.*, *409*, 251–271.

Mainprice, D., G. Barruol, and W. Ben Ismaïl (2000), The seismic anisotropy of the Earth's mantle: from single crystal to polycrystal., in *Earth's Deep Interior: Mineral Physics and Tomography from the Atomic to the Global Scale*, edited by S. I. Karato, pp. 237–264, Geodyn. Ser. AGU, Washington, D. C.

Mancilla, F. d. L., G. Booth-Rea, D. Stich, J. V. Pérez-Peña, J. Morales, J. M. Azañón, R. Martin, and F. Giaconia (2015), Slab rupture and delamination under the Betics and Rif constrained from receiver functions, *Tectonophysics*, *663*, 225–237.

Marchesi, C., C. J. Garrido, D. Bosch, J.-L. Bodinier, K. Hidas, J. A. Padron-Navarta, and F. Gervilla (2012), A late Oligocene suprasubduction setting in the westernmost Mediterranean revealed by intrusive pyroxenite dikes in the Ronda peridotite (Southern Spain), *J. Geol.*, *120*(2), 237–247.

Martinez-Martinez, J. M., J. I. Soto, and J. C. Balanya (2002), Orthogonal folding of extensional detachments: Structure and origin of the Sierra Nevada elongated dome (Betics, SE Spain), *Tectonics*, *21*(3), 1012, doi:10.1029/2001TC001283.

Mercier, J. C. C., and A. Nicolas (1975), Textures and fabrics of upper-mantle peridotites as illustrated by xenoliths from basalts, *J. Petrol.*, *16*(1), 454–487.

Naze, L., N. Doukhan, J. C. Doukhan, and K. Latrous (1987), A TEM study of lattice-defects in naturally and experimentally deformed orthopyroxenes, *Bull. Mineral.*, *110*(5), 497–512.

Negredo, A. M., P. Bird, C. Sanz de Galdeano, and E. Buforn (2002), Neotectonic modeling of the Ibero-Maghrebian region, *J. Geophys. Res.*, *107*(B11), 2292, doi:10.1029/2001JB000743.

Nicolas, A., and N. Christensen (1987), Formation of anisotropy in upper mantle peridotites—A review, in *Composition, Structure and Dynamics of the Lithosphere-Asthenosphere System*, *Geodyn. Ser.*, edited by K. Fuchs and C. Froidevaux, pp. 111–123, AGU, Washington, D. C.

Nimis, P., and H. Grütter (2010), Internally consistent geothermometers for garnet peridotites and pyroxenites, *Contrib. Mineral. Petrol.*, *159*(3), 411–427.

Obata, M. (1980), The Ronda peridotite-garnet-lherzolite, spinel-lherzolite, and plagioclase-lherzolite facies and the P-T trajectories of a high temperature mantle intrusion, *J. Petrol.*, *21*(3), 533–572.

O'Neill, H. S. C. (1981), The transition between spinel lherzolite and garnet lherzolite, and its use as a geobarometer, *Contrib. Mineral. Petrol.*, *77*(2), 185–194.

Pearson, D. G., and G. M. Nowell (2004), Re–Os and Lu–Hf isotope constraints on the origin and age of pyroxenites from the Beni Bousera peridotite massif: Implications for mixed peridotite–pyroxenite mantle sources, *J. Petrol.*, *45*(2), 439–455.

Platt, J. P., W. M. Behr, K. Johanesen, and J. R. Williams (2013), The Betic-Rif arc and its orogenic hinterland: A review, *Annu. Rev. Earth Planet. Sci.*, *41*(1), 313–357.

Plomerová, J., G. Payo, and V. Babuška (1993), Teleseismic P-residual in the Iberian Peninsula, *Tectonophysics*, *221*(1), 1–12.

Precigout, J., F. Gueydan, C. J. Garrido, N. Cogne, and G. Booth-Rea (2013), Deformation and exhumation of the Ronda peridotite (Spain), *Tectonics*, *32*, 1011–1025, doi:10.1002/tect.20062.

Rampone, E., R. L. M. Vissers, M. Poggio, M. Scambelluri, and A. Zanetti (2010), Melt migration and intrusion during exhumation of the Alboran lithosphere: The Tallante mantle xenolith record (Betic Cordillera, SE Spain), *J. Petrol.*, *51*(1–2), 295–325.

Serrano, I., T. M. Hearn, J. Morales, and F. Torcal (2005), Seismic anisotropy and velocity structure beneath the southern half of the Iberian Peninsula, *Phys. Earth Planet. Inter.*, *150*(4), 317–330.

Shimizu, Y., S. Arai, T. Morishita, H. Yurimoto, and F. Gervilla (2004), Petrochemical characteristics of felsic veins in mantle xenoliths from Tallante (SE Spain): An insight into activity of silicic melt within the mantle wedge, *Trans. R. Soc. Edinburgh: Earth Sci.*, *95*, 265–276.

Shimizu, Y., S. Arai, T. Morishita, and Y. Ishida (2008), Origin and significance of spinel–pyroxene symplectite in lherzolite xenoliths from Tallante, SE Spain, *Mineral. Petrol.*, *94*(1–2), 27–43.

Silver, P. G. (1996), Seismic anisotropy beneath the continents: Probing the depths of geology, *Annu. Rev. Earth Planet. Sci.*, *24*(1), 385–432.

Silver, P. G., D. Mainprice, W. Ben Ismail, A. Tommasi, and G. Barruol (1999), Mantle structural geology from seismic anisotropy, in *Mantle Petrology: Field Observations and High Pressure Experimentation: A Tribute to Francis R. (Joe) Boyd*, *Geochem. Soc. Spec. Publ. 6*, edited by Y. Fei, C. Bertka, and B. Mysen, pp. 79–103, The Geochem. Soc., Houston, Tex.

Soustelle, V., A. Tommasi, J. L. Bodinier, C. J. Garrido, and A. Vauchez (2009), Deformation and reactive melt transport in the mantle lithosphere above a large-scale partial melting domain: The Ronda peridotite massif, southern Spain, *J. Petrol.*, *50*(7), 1235–1266.

Soustelle, V., A. Tommasi, S. Demouchy, and D. A. Ionov (2010), Deformation and fluid–rock interaction in the supra-subduction mantle: Microstructures and water contents in peridotite xenoliths from the Avacha volcano, Kamchatka, *J. Petrol.*, *51*(1–2), 363–394.

Spakman, W., and R. Wortel (2004), A tomographic view on western Mediterranean geodynamics, in *The TRANSMED Atlas—The Mediterranean Region From Crust to Mantle*, edited by W. Cavazza et al., pp. 31–52, Springer-Verlag Berlin Heidelberg, Berlin.

Stich, D., E. Serpelloni, F. d. L. Mancilla, and J. Morales (2006), Kinematics of the Iberia-Maghreb plate contact from seismic moment tensors and GPS observations, *Tectonophysics*, *426*(3–4), 295–317.

Suhr, G. (1993), Evaluation of upper mantle microstructures in the Table Mountain massif (Bay of Islands ophiolite), *J. Struct. Geol.*, *15*(11), 1273–1292.

Taylor, W. R. (1998), An experimental test of some geothermometer and geobarometer formulations for upper mantle peridotites with application to the thermobarometry of fertile lherzolite and garnet websterite, *Neues Jahrb. Mineral., Abh.*, *172*(2–3), 381–408.

Tommasi, A., and A. Vauchez (2015), Heterogeneity and anisotropy in the lithospheric mantle, *Tectonophysics*, *661*, 11–37.

Tommasi, A., B. Tikoff, and A. Vauchez (1999), Upper mantle tectonics: Three-dimensional deformation, olivine crystallographic fabrics and seismic properties, *Earth Planet. Sci. Lett.*, *168*(1–2), 173–186.

Tommasi, A., D. Mainprice, G. Canova, and Y. Chastel (2000), Viscoplastic self-consistent and equilibrium-based modeling of olivine lattice preferred orientations: Implications for the upper mantle seismic anisotropy, *J. Geophys. Res.*, *105*, 7893–7908, doi:10.1029/1999JB900411.

Tommasi, A., M. Godard, G. Coromina, J. M. Dautria, and H. Barsczus (2004), Seismic anisotropy and compositionally induced velocity anomalies in the lithosphere above mantle plumes: A petrological and microstructural study of mantle xenoliths from French Polynesia, *Earth Planet. Sci. Lett.*, *227*(3–4), 539–556.

Tommasi, A., A. Vauchez, and D. A. Ionov (2008), Deformation, static recrystallization, and reactive melt transport in shallow subcontinental mantle xenoliths (Tok Cenozoic volcanic field, SE Siberia), *Earth Planet. Sci. Lett.*, *272*(1–2), 65–77.

Tommasi, A., M. Knoll, A. Vauchez, J. Signorelli, C. Thoraval, and R. Loge (2009), Structural reactivation in plate tectonics controlled by olivine crystal anisotropy, *Nat. Geosci.*, *2*(6), 422–426.

Torné, M., M. Fernandez, M. C. Comas, and J. I. Soto (2000), Lithospheric structure beneath the Alboran Basin: Results from 3D gravity modeling and tectonic relevance, *J. Geophys. Res.*, *105*, 3209–3228, doi:10.1029/1999JB900281.

Turner, S. P., J. P. Platt, R. M. M. George, S. P. Kelley, D. G. Pearson, and G. M. Nowell (1999), Magmatism associated with orogenic collapse of the Betic–Alboran domain, SE Spain, *J. Petrol.*, *40*(6), 1011–1036.

Van der Wal, D., and R. L. M. Vissers (1996), Structural petrology of the Ronda peridotite, SW Spain: Deformation history, *J. Petrol.*, *37*(1), 23–43.

Vauchez, A., and C. J. Garrido (2001), Seismic properties of an asthenospherized lithospheric mantle: Constraints from lattice preferred orientations in peridotite from the Ronda massif, *Earth Planet. Sci. Lett.*, *192*(2), 235–249.

Vauchez, A., and A. Nicolas (1991), Mountain building—Strike-parallel motion and mantle anisotropy, *Tectonophysics*, *185*(3–4), 183–201.

Vauchez, A., A. Tommasi, and D. Mainprice (2012), Faults (shear zones) in the Earth's mantle, *Tectonophysics*, *558*, 1–27.

Vollmer, F. W. (1990), An application of eigenvalue methods to structural domain analysis, *Geol. Soc. Am. Bull.*, *102*(6), 786–791.

Witt-Eickschen, G., and H. A. Seck (1991), Solubility of Ca and Al in orthopyroxene from spinel peridotite—An improved version of an empirical geothermometer, *Contrib. Mineral. Petrol.*, *106*(4), 431–439.

Wright, S. I., M. M. Nowell, and D. P. Field (2011), A review of strain analysis using electron backscatter diffraction, *Microsc. Microanal.*, *17*(3), 316–329.

Zhang, S. Q., and S. Karato (1995), Lattice preferred orientation of olivine aggregates deformed in simple shear, *Nature*, *375*(6534), 774–777.